Published in final edited form as:
Cell Rep. 2023 November 28; 42(11): 113423. doi:10.1016/j.celrep.2023.113423.

Jedi-1/MEGF12-mediated phagocytosis controls the pro-neurogenic properties of microglia in the ventricular-subventricular zone

Vivianne Morrison[1,5,10], **Matthew Houpert**[1,5], **Jonathan Trapani**[1,5], **Asa Brockman**[2,5], **Philip Kingsley**[1], **Ketaki Katdare**[5], **Hillary Layden**[1], **Gabriela Nguena-Jones**[1,5], **Alexandra Trevisan**[1,6], **Kathleen Maguire-Zeiss**[7], **Lawrence Marnett**[1,3,4,8], **Gregory Bix**[9], **Rebecca Ihrie**[2,5], **Bruce Carter**[1,5,11,*]

[1]Department of Biochemistry, Vanderbilt University, Nashville, TN 37232, USA

[2]Department of Cell and Developmental Biology, Vanderbilt University, Nashville, TN 37235, USA

[3]Department of Chemistry, Vanderbilt University, Nashville, TN 37235, USA

[4]Department of Pharmacology, Vanderbilt University, Nashville, TN 37235, USA

[5]Vanderbilt Brain Institute, Vanderbilt University, Nashville, TN 37235, USA

[6]Department of Developmental Neurobiology, St. Jude Children's Research Hospital, Memphis, TN 38105, USA

[7]Department of Neuroscience, Georgetown University, Washington, DC 20057, USA

[8]A.B. Hancock Jr. Memorial Laboratory for Cancer Research, Vanderbilt-Ingram Cancer Center, Nashville, TN 37232, USA

[9]Center for Clinical Neuroscience Research, Tulane University, New Orleans, LA 70118, USA

[10]Department of Cell and Molecular Biology, Tulane University, New Orleans, LA 70118, USA

[11]Lead contact

---

[*]Correspondence: bruce.carter@vanderbilt.edu.

AUTHOR CONTRIBUTIONS

V.M. and B.C. conceptualized the project. V.M., M.H., J.T., and K.K. performed the immunostainings and quantification. G.N.-J. assisted with the apoptotic cell quantification. V.M., J.T., and B.C. carried out the *in vitro* engulfment assays. K.M.-Z. helped with the microglia dissections and consulted throughout the project. M.H. isolated the microglia and generated the RNA-sequencing data, and H.L. assisted with the data and statistical analyses. A. B., V.M., M.H., and R.I. performed the proliferation analyses in the V-SVZ and IL-1β blocking experiment and analyses. A.T. generated the Jedi-1 knockout and floxed mice. P.K. and V.M. generated the lipid and prostaglandin data, with consultation and assistance from L.M. G.B. provided critical input into the study and feedback on writing of the manuscript. The manuscript was written by V.M. and B.C. with contributions from all co-authors.

SUPPLEMENTAL INFORMATION

Supplemental information can be found online at https://doi.org/10.1016/j.celrep.2023.113423.

DECLARATION OF INTERESTS

The authors declare no competing interests.

INCLUSION AND DIVERSITY

One or more of the authors of this paper self-identifies as an underrepresented ethnic minority in their field of research or within their geographical location. One or more of the authors of this paper self-identifies as a gender minority in their field of research. One or more of the authors of this paper self-identifies as a member of the LGBTQIA+ community. One or more of the authors of this paper self-identifies as living with a disability.

SUMMARY

Microglia are the primary phagocytes in the central nervous system and clear dead cells generated during development or disease. The phagocytic process shapes the microglia phenotype, which affects the local environment. A unique population of microglia resides in the ventricular-subventricular zone (V-SVZ) of neonatal mice, but how they influence the neurogenic niche is not well understood. Here, we demonstrate that phagocytosis contributes to a pro-neurogenic microglial phenotype in the V-SVZ and that these microglia phagocytose apoptotic cells via the engulfment receptor Jedi-1. Deletion of *Jedi-1* decreases apoptotic cell clearance, triggering a neuroinflammatory microglia phenotype that resembles dysfunctional microglia in neurodegeneration and aging and that reduces neural precursor proliferation via elevated interleukin-1β signaling; interleukin-1 receptor inhibition rescues precursor proliferation *in vivo*. Together, these results reveal a critical role for Jedi-1 in connecting microglial phagocytic activity to the maintenance of a pro-neurogenic phenotype in the developing V-SVZ.

Graphical abstract

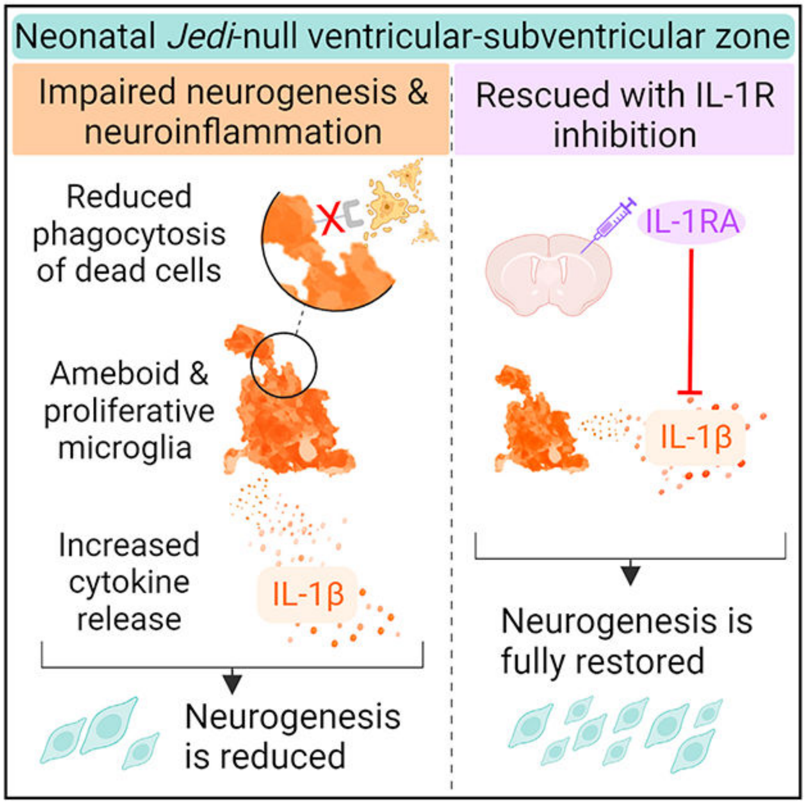

In brief

Morrison et al. demonstrate that microglia in the neonatal ventricular-subventricular zone express the phagocytic receptor Jedi-1 to dispose of dead cells. Moreover, Jedi-1 mitigates an inflammatory phenotype in this neurogenic niche, such that loss of Jedi-1 results in neuroinflammatory microglia that suppress neurogenesis. However, neurogenesis is rescued by inhibiting interleukin-1β.

INTRODUCTION

Microglial phagocytosis is critical for sculpting the developing central nervous system (CNS), and whether in health or disease, microglia eliminate potentially inflammatory substrates such as dead cells, myelin debris, and protein aggregates.[1] In disease states, the signaling cascades that are triggered by receptor-mediated phagocytosis help generate distinct microglia phenotypes with transcriptomic, morphological, and functional features that are context specific.[2–5] Triggering receptor expressed on myeloid cells 2 (TREM2) is a prime example of this relationship. TREM2 modulates microglia characteristics including but not limited to morphology, proliferation, migration, lipid metabolism, cytokine production, and phago-lysosomal pathways.[2,3] Evidence suggests that a similar relationship may exist in the healthy brain, specifically in the adult hippocampal neurogenic niche,[6,7] but it is not fully understood to what extent this process can be generalized to other environments and time points that also demand substantial debris clearance and inflammatory pathway regulation, such as in the neonatal ventricular-subventricular zone (V-SVZ) neurogenic niche and developing white matter. This seems a likely scenario, given that V-SVZ-resident neonatal microglia display a genetic signature resembling that of microglia populations that are found in disease and whose phenotypes are influenced by phagocytosis.[4,5,8,9] The degree of microglial phagocytosis in the neonatal V-SVZ as well as whether it plays a role in generating this region's unique microglial phenotype or contributes to neurogenesis has not been explored.

Neurogenesis is the production of neural precursor cells (NPCs) and immature neurons (neuroblasts), with as many as 30,000 NPCs produced per day in the adult mouse V-SVZ.[10] Many newborn cells undergo apoptosis (an estimated 60%[11–14]) as part of a normal culling process that is necessary for the maintenance of tissue organization and to prevent excessive cell numbers.[15,16] Thus, there is a substantial number of dead cells in the V-SVZ, and it is presumed that V-SVZ-resident microglia engulf and dispose of the debris.[17] Disruption of microglial function, though not specifically of phagocytosis, negatively impacts NPC proliferation, neuronal differentiation, and survival, suggesting that neonatal V-SVZ-resident microglia support the neurogenic program.[17–19] Whether their pro-neurogenic functions are related to their phagocytic ability remains to be determined.

While findings from adult animals cannot always be generalized to the developing brain, studies in the adult V-SVZ and hippocampal subgranular zone (SGZ) suggest that microglial phagocytosis does influence neurogenesis. For example, the deletion of TAM (Tyro3/Axl/MerTK) receptor family members and members of the P2Y family of purine-responsive engulfment receptors not only impacts microglial characteristics such as morphology but also leads to the accumulation of dead cells in the SGZ, the V-SVZ, and the rostral migratory stream (RMS) (i.e., the path that neuroblasts follow to their primary destination, the olfactory bulb) and to fluctuations in the rates of NPC proliferation and neuronal differentiation.[7,20] Transcriptomic profiling of phagocytic microglia *in vitro* suggests that widespread changes in the cells' secretome account for the pro-neurogenic influence of phagocytic microglia in the adult SGZ.[7] Taken together, these results suggest a connection between microglial phagocytic ability and neurogenesis, but the exact nature of the relationship and its underlying mechanisms remain to be determined in both the adult and, to an even greater extent, the neonatal neurogenic niches.

Importantly, with the arrival of single-cell RNA sequencing, it is clear that microglia exist in a wide variety of functional states.[21] We use several frequently cited acronyms, which we will define below, but it must be acknowledged that these abbreviations are used solely for simplicity and do not necessarily represent the true extent of microglia diversity.

In the neonatal period, microglia found in the V-SVZ and developing white matter are called “proliferative region-associated microglia” (PAMs).[9] In adults, a variety of transcriptomically distinct populations have been described in specific contexts and are often described in terms of how their genetic signatures differ from that of adult homeostatic microglia. For the purposes of this work, the relevant adult populations include “disease-associated microglia” (DAMs),[3,4] neurodegenerative microglia (MGnD),[22] and “disease inflammatory microglia” (DIMs).[5] In general, the DAM and MGnD populations exhibit neuroprotective properties, while DIMs likely contribute to maladaptive responses to neurodegeneration and functional decline.[5,8] Previous literature has demonstrated a connection between neurodegeneration and dysfunctional engulfment and processing of engulfed material, suggesting that phagocytosis is a protective measure that restricts inflammatory activation of microglia.[23–25]

Overall, phagocytosis appears to be a lens through which microglia see their environment and make phenotypic changes based on the specific needs of that environment. Therefore, a defect in this lens can have sweeping detrimental effects on the core processes of a given context, such as neurogenesis in the V-SVZ. To further explore this topic, we investigated the role of the engulfment receptor Jedi-1 in V-SVZ-resident microglia. Jedi-1 (aliases: MEGF12 and PEAR1, hereafter referred to as “Jedi”) is a mammalian homolog of the engulfment receptors draper and CED-1 in flies and nematodes, respectively.[26] Characterization of Jedi in the developing peripheral nervous system revealed its role in promoting the clearance of apoptotic sensory neurons by adjacent satellite glial precursors and its execution of this process by the same intracellular signaling motifs as those used in TREM2-DAP12 signaling.[26–28] However, the role of Jedi in the CNS has never been explored.

RESULTS

Microglia express Jedi both *in vivo* and *in vitro*

Jedi transcripts in neonatal microglia have been detected by several single-cell RNA-sequencing studies,[8,9,29] and given that Jedi is important for engulfing dead cells, we hypothesized that Jedi protein in microglia would be most highly expressed in the V-SVZ, a region with high cell turnover. On average, we found that Jedi co-localized with at least 43% of IBA1$^+$ microglia cell bodies in the dorsal V-SVZ (Table S1). Jedi was also present in numerous microglia processes and phagocytic cups, frequently overlapping with pyknotic nuclei in the dorsal V-SVZ and corpus callosum (CC) (Figures 1A–1E). This pattern of Jedi-IBA1 co-localization differed from that seen in the ventral V-SVZ and surrounding area (corresponding roughly to the RMS), which was largely diffuse (Figures 1F–1H).

Co-labeling was sparse in the striatum and septum and not detected in the cortex (Figures S1A–S1E). Beyond microglia, Jedi expression was localized to blood vessels, which has been reported in peripheral tissues,[30] and staining intensity was highest among vessels in and around the neurogenic niche and the septum; vascular Jedi staining was conspicuously absent from all but layer I of the cortex, and even then, staining was less dramatic than that found deeper in the cerebrum (Figure S1A).

Recent RNA-sequencing data show *Jedi* expression in microglia cultured from postnatal day 5 (P5) wild-type (WT) mice,[31] and we also observed Jedi protein in mixed glial cultures, with variable intensity and staining patterns like those observed in the brain. Jedi was detected in microglia processes and phagocytic cups associated with pyknotic nuclei of neighboring glia (Figure 2A) as well as in the ruffled membranes of microglia not actively engulfing dead cells (Figure 2B). In contrast, Jedi staining in microglia-enriched cultures was more homogeneous, much in the same way that cellular morphology is more homogeneous in these highly pure cultures (Figures 2C and S2). We found that just over 40% of cells expressed Jedi after 1 day in monoculture, but only at low levels; however, this constituted a dramatic divergence from the polarized staining pattern that we observed in microglia in mixed glia cultures. Overall, Jedi signal intensity and staining pattern are variable in microglia in the neurogenic niche and developing white matter, with strong regional differences *in vivo* as well as in cultured conditions. Our finding that 43% of V-SVZ microglia express Jedi was based on somatic co-localization of Jedi and IBA1. However, given the number of times that the Jedi signal was found to overlap with microglia processes, the true number of Jedi-expressing microglia in the V-SVZ may be even higher, and quantification could fluctuate as a function of changes in cell morphology. Together, these findings suggest that Jedi expression in microglia is highly specific to the cell's environment and, given that the strongest expression coincides with the presence of dead cells in the V-SVZ/CC and mixed glia cultures, Jedi likely supports engulfment activities in microglia.

Indeed, in an *in vitro* engulfment assay that exposes microglia to negatively charged carboxylated latex beads to mimic phosphatidylserine, an established "eat-me" signal[32] (Figures 2D–2F), fewer microglia performed bead engulfment in *Jedi*-null (JKO) cultures relative to WT (Figure 2G), and those cells that did engulf beads performed significantly worse than did WT microglia, as measured by the phagocytic index, a score that combines an approximate measure of "engulfed beads per cell" with the percentage of microglia performing engulfment (Figure 2H). Even the degree to which *Jedi*-null microglia captured and retained beads on the cell surface was reduced, as measured by a variation of the phagocytic index that we termed the "bead-binding index" (Figure 2I). All these measures showed a time-dependent increase in bead engulfment even in the absence of Jedi, pointing to the likely presence of Jedi-independent engulfment pathways. Nonetheless, in all three measures, the degree of increase between time points was smaller in JKO microglia than in WT cells. These findings raised the possibility that microglia engulfment capacity *in vivo* would be reduced in *Jedi*-null animals.

Jedi deficiency reduces dead cell engulfment and clearance while triggering a neuroinflammatory phenotype in V-SVZ microglia

Using the TUNEL assay to label cleaved DNA in apoptotic cells, we found a statistically significant increase in the number of TUNEL$^+$ puncta in the V-SVZ of JKO mice relative to WT (Figures 3A–3C). However, the numbers of dead cells found in the cortex and striatum of JKO mice were not significantly different from those of WT mice (Figures 3D–3G). The increase in dead cells was accompanied by a decrease in the fraction of those cells that were engulfed by *Jedi*-null microglia (Figures 3H–3K). These results, together with the immunostaining findings, indicate a positive correlation between the presence of dead cells and Jedi expression, suggesting that apoptotic debris may trigger an increase in Jedi expression above baseline levels or increase its localization to the cell membrane in preparation for engulfment. This may be why Jedi protein is detected in so few microglia outside of the V-SVZ and CC, in regions with very low levels of cell turnover, and it also provides an explanation for why dead cells do not accumulate in the cortex and striatum of *Jedi*-null microglia.

On the other hand, the degree of IBA1 staining, the density of microglia in the JKO V-SVZ, and their ameboid morphology (as measured by the circularity index, where 1.0 indicates a perfect circle[33]) were significantly increased relative to the same measures in WT V-SVZ microglia (Figures 4A–4I). Microglial morphology generally correlates with state changes, and non-homeostatic microglia are rounder (“ameboid”) and have fewer processes than homeostatic microglia.[34] Taken together, the simultaneous increase in microglia density and the accumulation of dead cells argues strongly for a defect in phagocytosis *in vivo* but does not preclude an increase in cell death among NPCs. The fact that microglia were more numerous in the JKO V-SVZ was due in part to an increase in proliferation because the number of microglia that incorporated 5-ethynyl-2′-deoxyuridine (EdU) into newly synthesized DNA after cell division was significantly higher among *Jedi*-null microglia (Figures 4J–4L). Together, these measures reflect a shift toward an inflammatory state, suggesting that Jedi-mediated engulfment helps regulate microglia phenotype in the V-SVZ. Typically, phagocytic activity increases in parallel with these hallmarks of an inflammatory phenotype, but this does not occur in *Jedi*-null microglia, highlighting that alternative mechanisms of dead cell engulfment and clearance are not sufficient to overcome the loss of Jedi.

However, microglia number, shape, and degree of proliferation cannot provide a deeper understanding of how microglia phenotype is altered by the loss of Jedi. Therefore, we performed differential gene expression analyses in highly pure microglia selected via anti-CD11b magnetic beads sorting (Figure S3), comparing V-SVZ microglia between JKO and WT pups, and found that the phenotypic changes were paralleled by statistically significant upregulation of genes associated with inflammatory pathway activation (Figures 5A, 5B, 5D, and 5F). Moreover, genes associated with the PAM/DAM, MGnD, and DIM populations were differentially upregulated, although only the DIM genes reached statistical significance, owing to variability in PAM/DAM and MGnD gene expression between biological replicates in both the WT and JKO groups (Figures 5B, 5F, 5G, S4C, and S4E). In alignment with previously published single-cell RNA-sequencing datasets,[8,9] WT V-SVZ microglia have higher expression of PAM/DAM genes than WT microglia derived from the cortex (Figures S4A and S4B).

Incidentally, we found that the expression of adult homeostatic microglia genes is decidedly mixed in V-SVZ microglia from WT animals and varies in WT cortical microglia also, but to a lesser extent (Figure S4C). Single-cell RNA-sequencing studies show a relative downregulation of these genes between neonates and adults[2,4,8,9] but are of limited utility when interpreting our data because we assess regional differences rather than those that occur between ages. Nonetheless, the expression profile of adult homeostatic microglia markers in WT V-SVZ microglia contrasts with the upregulation that we observed in JKO V-SVZ microglia (Figures 5B and 5F). This was unexpected given that the samples are from neonatal animals and that the adult homeostatic microglial signature differs so remarkably from the DIM signature, which is over-represented in JKO V-SVZ microglia. The MGnD population, which was recently characterized, also has neuroprotective qualities,[22,35] but most MGnD markers in the JKO microglia did not achieve a significant fold change or adjusted p value (Figures S4C and S4D). Overall, upregulation of the adult homeostatic and DIM gene cassettes as well as pathways associated with neuroinflammation were among the most consistent and significant changes seen in JKO V-SVZ microglia. Still, some genes associated with negatively regulating inflammation (e.g., *Tgfbr1* and *Il10ra*) were modestly but significantly increased in JKO microglia, which is suggestive of attempts to mitigate chronic inflammatory pathway activation. This idea has been raised by others in the contexts of MGnDs[22] and DIMs *in vivo* and after chronic stimulation of microglia *in vitro* with pro-inflammatory agents.[5,36] Whether the changes we found reflect a mixed transcriptomic state of individual microglia, a diversification of the V-SVZ microglia population, or some combination of these scenarios cannot be discerned from bulk RNA sequencing.

Nonetheless, key changes at the transcriptomic level, such as increased expression of *Nlrp3* and *Il1b* as well as of *Ptgs1* and *Pla2g3*, which are involved in lipid mediator metabolism, were also detectable at the level of soluble inflammatory mediators. In microdissected V-SVZ, levels of the canonical inflammatory cytokine interleukin-1β (IL-1β) were significantly elevated in JKO tissue (Figure 5H). *Ptgs1* and *Pla2g3* regulate the synthesis of prostaglandins (PGs) and fatty acids such as lysophosphatidylcholine (LPC), both of which can be associated with increasing inflammation, although the nature of this association may depend on the context.[37] Fifteen lipid analytes were measured in microdissected V-SVZ, and significant increases were found for 16:0 LPC, PGE_2, and PGD_2 (Figures 5I–5K). Endocannabinoids and related species are implicated in regulating inflammatory pathways in microglia,[38] and we found that oleoylethanolamide (OEA), an analog of anandamide, was significantly elevated in V-SVZ tissue from JKO animals (Table S1). OEA activates peroxisome proliferator-activated receptor α, which is associated with reducing inflammatory markers in microglia,[39] raising the possibility that increased OEA synthesis may be another attempt to reduce inflammation in the JKO V-SVZ.

Deficient phagocytic activity was a significant part of the phenotypic changes that we observed in JKO V-SVZ microglia. Indeed, RNA sequencing revealed that numerous transcripts that are produced by NPCs, neurons, and glia were significantly depleted in JKO V-SVZ microglia compared to WT (Figures 5B, 5C, and 5E). This aligns with the observation that microglia become enriched for genes associated with neurogenesis after they engulf apoptotic neural cells[7] and that PAMs engulf developing oligodendrocytes in the CC.[9] Together, our results strongly suggest that Jedi is integral to the phagocytic properties of V-SVZ microglia as well as to their molecular identities and/or the composition of the V-SVZ microglia population. Specifically, the cells likely rely on Jedi-dependent signaling to regulate inflammatory gene expression in the presence of dead cell debris, which we showed is elevated in the V-SVZ relative to neighboring regions.

Intuitively, these changes in microglia phenotype and phagocytic ability likely follow the loss of Jedi signaling in microglia. Our immunofluorescence studies showed that Jedi is highly expressed by vasculature in the V-SVZ, raising the possibility that blood vessels play a role in the JKO phenotype. While we cannot rule out vascular involvement, we found that acute loss of *Jedi* specifically in microglia of $Cx3cr1^{CreERT2/+}$;$Jedi^{flox,flox}$ pups was sufficient to recapitulate increases in the degree of IBA1 expression and ameboid morphology among V-SVZ microglia (Figures 6A–6F and S5). In contrast to mice with a germline deletion of *Jedi*, $Cx3cr1^{CreERT2/+}$;$Jedi^{flox/flox}$ microglia-specific JKO mice (mJKOs) did not have significantly more dead cells in the V-SVZ than control littermates (Table S1).

Defective neurogenesis in the absence of microglial Jedi is a result of increased IL-1β signaling

We have shown that JKO microglia adopt a neuroinflammatory phenotype, and we observed an increase in IL-1β protein in the JKO V-SVZ. It is well established that inflammatory factors, particularly IL-1β, negatively impact neurogenesis.[40–43] We found that the number of NPCs generated in the JKO V-SVZ as well as the number of proliferating NPCs were significantly lower than in WT V-SVZ (Figures 7A–7D). Furthermore, the overall number of proliferating cells in the JKO V-SVZ was reduced (Figure 7E). Crucially, acute microglia-specific deletion of *Jedi* was sufficient to recapitulate the global knockout neurogenesis defect in every way (Figures 7F–7J). Importantly, intracortical administration of a recombinant IL-1β receptor antagonist at P4 completely rescued the JKO neurogenesis defect by P7, demonstrating that the regulation of IL-1β activity is a critical link between Jedi function in microglia and neurogenesis in the V-SVZ (Figures 7K–7O and S6).

DISCUSSION

Phagocytosis underlies the link between microglia phenotype and neurogenesis

Microglia are key players in regulating CNS homeostasis in diverse contexts. These cells are exquisitely sensitive to their environment, in part by virtue of the material that they phagocytose, and rapid phenotypic shifts ensure timely and targeted responses to external changes. Few studies have examined the extent to which phagocytosis by microglia influences neurogenesis. *In vivo* work has focused on TAM and purinergic receptor deletion (*Tyro3/Axl/Mertk* and *P2ry12*, respectively), and, due in part to methodological differences as well as to biologically relevant differences between ages and brain regions, the studies reached slightly different conclusions. Fourgeaud et al. reported that adult (3- to 6-month-old) *Axl/Mertk*-null mice accumulated dead cells in the V-SVZ and RMS but had more newly generated neurons in the olfactory bulb[20]; in contrast, Ribeiro Xavier et al. reported that microglia in the V-SVZ and RMS of juvenile mice (1–2 months old) showed no evidence of phagocytosis of neurogenic cells, and, in fact, TREM2 and P2Y-family receptor expression in microglia was absent or very low in these regions[18]; Ji et al. found that loss of TAM receptors reduced NPC proliferation and survival and, independently, reduced neuronal differentiation in the adult SGZ[44,45]; and Diaz-Aparicio et al. demonstrated that deletion of *Mertk/Axl* or *P2ry12* affected SGZ neurogenesis but with divergent outcomes, and the divides between these outcomes were further widened when comparing acute deletions with germline deletions.[7] Despite their differences, these previous studies are generally in line with our finding that neurogenesis is closely tied to microglia phenotype, which itself is a product of phagocytic activity. It is important to note that in all cases, the targeted deletion of one or two engulfment receptors did not completely abrogate phagocytic activity, which aligns with our findings. The presence of multiple pathways points to the importance of phagocytosis as well as to the possibility that engulfment pathways display selectivity in terms of what material they engulf, which has been shown to occur in dendritic cells (e.g., an apoptotic cell versus a necrotic cell, early versus late apoptotic/secondary necrotic cells).[46–48]

According to single-cell RNA-sequencing datasets, PAMs coexpress a variety of engulfment receptors[8] although for the most part their expression profile and functions have not been explored. Our pathway analysis of JKO microglia returned six terms involving phagocytosis, and phagocytosis-related genes that were identified in the MGnD population showed some increases in JKO V-SVZ microglia, although they did not reach significance because of within-group variability. Nevertheless, there was no significant functional compensation for the absence of Jedi. In both our *in vitro* and *in vivo* engulfment analysis, we observed the presence of phagocytic microglia in the JKO samples, which is consistent with previous findings that deletion of *Axl/Mertk* or *P2ry12* did not completely abrogate microglial phagocytic ability. The various engulfment receptors expressed by microglia are likely independent and/or complementary and may provide additional precision in microglia responses to specific stimuli. Additionally, engulfment receptors belong to an array of families and activate different signaling modalities that are likely to further increase the granularity and relevance of microglial interactions with the events occurring around them. For example, Axl and MerTK are receptor tyrosine kinases, P2RY12 is a G-protein-coupled receptor, TREM2 signals via immunoreceptor tyrosine-based activation motifs (ITAMs) in its co-receptor, DAP12, and similarly, Jedi signals via ITAMs in its intracellular domain.

Neurogenesis and the microglia “secretome”

Several studies point to the body of secreted factors as a key determinant of the phenotypic changes that occur after phagocytosis. Fortunately, significant progress has been made in characterizing the composition of the phagocytic secretome, which includes cytokines, signaling lipids, growth factors, and more.[7]

Cytokines are the most likely mechanism of microglial influence on NPC function, and IL-1β has been implicated in microglia-associated changes in neurogenesis. For example, TAM receptor-null microglia increased the expression of canonical inflammatory molecules, including IL-1β, which coincided with decreased SGZ neurogenesis,[44] and persistent overexpression of IL-1β in WT adults impaired hippocampal neurogenesis.[49] *In vitro*, microglia-derived IL-1β promoted neurogenesis at low concentrations (1 ng/mL) but had the opposite effect at higher concentrations (10 ng/mL).[36,40] In agreement with this, we showed that IL-1β levels were elevated in the JKO V-SVZ and that blocking IL-1β signaling rescued NPC proliferation in JKO mice. Thus, we were able to directly link faulty phagocytosis to defective neurogenesis via increased IL-1β secretion from V-SVZ-resident microglia *in vivo*. The link between defective phagocytosis and pathological increases of IL-1β is supported by several studies. In cultured microglia exposed to lipopolysaccharide (LPS), the typical robust expression of IL-1β, IL-6, and tumor necrosis factor α was significantly dampened by pre-treatment of the microglia with dead cell debris, and this suppression of inflammatory cytokines occurred without necessarily an accompanying increase in transforming growth factor β (TGF-β) or IL-10 production, although this may be context specific: increases in TGF-β, PGE_2, and nerve growth factor have also been observed after LPS stimulation of microglia that have ingested apoptotic cells.[50–53] We observed modest increases in *Tgfbr1* expression without changes in *Tgfb1* itself, but overall our observations agree with previous findings, emphasizing the role that Jedi plays in transducing an apoptotic cell-derived signal into an immunomodulatory phenotype that supports neurogenesis.

Additional mechanisms are likely at play and may involve lipid mediators, which we found to be altered in *Jedi*-null mice. Our lipidomic analysis focused on PGs, which are members of the eicosanoid family of arachidonic acid-derived lipid mediators, including thromboxanes and prostacyclins, all of which influence inflammation, sometimes in opposing ways.[54] Concomitant with the increase in IL-1β levels and the emergence of a neuroinflammatory genetic signature in JKO microglia, we observed a significant elevation in PGD_2 and PGE_2. In macrophages, ingestion of apoptotic cells induces cyclooxygenase-2 (COX-2)-dependent production of PGE_2, which in turn promotes the secretion of TGF-β, inducing a “tolerogenic” phenotype.[55] We were unable to reliably detect TGF-β in our V-SVZ lysates, and our sequencing dataset did not show differential expression of *Tgfb* or *Ptgs2* (COX-2) in JKO microglia. On the other hand, microglia-derived PGD_2 has been implicated in inflammation, demyelination, and astrogliosis both *in vitro* and *in vivo*.[56] PGD/E_2 can also be synthesized by COX-1 activity, and COX-1-derived PGs may have functions different from those of COX-2-derived PGs.[57] Whether these lipid mediators contribute to the JKO neuroinflammatory phenotype and subsequent neurogenesis defect or whether they play a part in a negative feedback loop to control neuroinflammation is not yet known. We also found an increase in LPC, which is notable because LPC is associated with NLRP3 inflammasome-dependent IL-1β synthesis.[58,59] We limited our analysis to several key lipid species but, given our current findings, a more comprehensive lipidomic analysis in the future will be beneficial to understanding the role that lipid mediators play in the *Jedi*-null microglial phenotype and neurogenesis deficit.

Limitations of the study

We provide evidence that Jedi plays a role in regulating microglia phenotype in the V-SVZ. However, there are caveats that limit our interpretations and that provide direction regarding necessary experiments to be performed in the future. First, there are remaining questions about Jedi expression. Some of these questions cannot fully be addressed with wide-field microscopy of immunofluorescent staining in fixed brain sections, which was the primary form of imaging used in our study. Despite the challenges of imaging live tissue, particularly when it is deep in the brain like the V-SVZ, live imaging is likely the best way to capture complex spatiotemporal relationships between Jedi, cell type, and the agile processes of neurogenesis and phagocytosis. Further, at this time we cannot say whether the pattern of Jedi expression that we observed in neonates persists in the adult, aging, injured, or diseased brain. It is likely, however, that Jedi expression increases, if not with age then with the appearance of neuropathology, because there are increases in neuronal senescence and cell death[8,60–63] and, thus, an increase in the amount of material to be engulfed and cleared.

Second, here we used bulk RNA sequencing to assess microglia phenotype, but without single-cell resolution we cannot differentiate between a scenario in which individual microglia adopt a mixed genetic signature and one in which the homogeneity of the V-SVZ-resident microglia population is lost and replaced with a variety of microglia phenotypes that develop *in situ* or arrive from outside the V-SVZ. Relatedly, without additional transcript tagging techniques, we cannot confidently say whether a read originates from the microglia itself or the engulfed cargo. This ambiguity precludes us from using our dataset for discovery-focused purposes. Therefore, for genes that met the thresholds for both statistical and biological significance but have not been characterized in microglia or in cells of neural lineages, we cannot yet make predictions about how they may or may not contribute to the JKO phenotype.

Third, we used an inducible *Cx3cr1-Cre* line to delete *Jedi* in microglia, but the extent of this line's cell-type specificity is a perennial issue, and other driver lines, such as the *Tmem119-Cre* line,[29,64–66] have been proposed with the goal of limiting deletion of the target gene in peripheral monocyte/macrophage-lineage cells, which also express *Cx3cr1*. However, the *Tmem119-2A-EGFP* reporter line shows *Tmem119* expression in vasculature-associated cells in neonatal mice,[29] so, for our purposes, the *Tmem119-Cre* line may not be the best alternative. Two studies in recent years have demonstrated changes in microglia and neural progenitors in the *Cx3cr1-Cre*^{ERT2} line following tamoxifen administration,[67,68] although between these studies and our own there are methodological differences (i.e., the method and timing of tamoxifen administration) that may account for the fact that their results do not align with our own. Namely, in their paradigm, it was found that tamoxifen administration in *Cx3cr1-Cre*^{ERT2} neonates caused a reduction in microglia cell number, increased cell death among microglia, increased phagocytosis by microglia, and increased morphological complexity.[67] For our part, we found an increase in microglia number, a decrease in morphological complexity, and a decrease in phagocytosis. Additionally, while tamoxifen administration during embryonic development severely impacts corticogenesis,[68] whether the postnatal treatment paradigm used in our study would have the same effects was not investigated. Still, at this time we cannot rule out the possibility that tamoxifen or *Cx3cr1-Cre*^{ERT2} induction influenced our findings. To address this, it will be necessary to comprehensively investigate mJKO microglia genetic signatures and engulfment ability *in vivo*, as was done for the global JKO. The challenges and controversies of *Cre*-driver leakiness and method of induction are widespread in the field, and these caveats must continue to be acknowledged when reporting and interpreting findings.

Finally, the most intuitive interpretation of our findings is that it is specifically the loss of Jedi-mediated phagocytosis that triggers the neuroinflammatory shift in V-SVZ microglia. However, as we do not yet know whether Jedi has functions beyond phagocytosis, an alternative interpretation is that the loss of Jedi triggers the shift independently from its role as a phagocytic receptor. Without the live imaging experiments described herein and without forced overexpression of another phagocytic pathway that could presumably compensate for the loss of Jedi-mediated phagocytosis, we cannot yet rule out this possibility. Future experiments that address these caveats will provide clarity and deepen our understanding not only of Jedi function but also of microglia identity and function in the developing brain.

STAR★METHODS

RESOURCE AVAILABILITY

Lead contact—Further information and requests for resources and reagents should be directed to and will be fulfilled by the lead contact, Bruce Carter (bruce.carter@vanderbilt.edu).

Materials availability—Mouse lines generated in this study will be available upon request.

Data and code availability

- RNA-seq data have been deposited at GEO and are publicly available as of the date of publication. Accession numbers are listed in the key resources table.
- This study did not generate any original code.
- Any additional information required to reanalyze the data reported in this paper is available from the lead contact upon request.

EXPERIMENTAL MODEL AND STUDY PARTICIPANT DETAILS

Animals—All animal procedures were performed in accordance with the Vanderbilt University Medical Center's comprehensive Animal Care and Use Program (ACUP) and NIH guidelines for the Care and Use of Laboratory Animals. Mice were housed under a controlled 12-h light/dark cycle and fed standard laboratory rodent diet (LabDiet, Cat#5001) with water available *ad libitum*. The day the pups were born was designated as postnatal day 0 (P0), and endpoint sample collection was performed at P7. We chose P7 as our endpoint because while the "neonatal" period extends from P0 to P28,[72] cell turnover and microglia density in the V-SVZ reach their apices.[9,17,73] Global *Jedi* knockout mice (JKO) were $Pear1^{tm1a(KOMP)Wtsi}$ mice derived from embryonic stem cells provided by the International Mouse Phenotype Consortium (IMPC, Cat#CSD31459_C05; RRID: MMRRC_060102-UCD). For comparisons involving the JKO line, the control animals were wild-type (WT) C57/BL6 mice (The Jackson Laboratory, RRID: IMSR_JAX:000664). A floxed *Jedi* line ($Jedi^{fl/fl}$) was generated by crossing JKO mice with the B6N.129S4-$Gt(ROSA)26Sor^{tm1(FLP1)Dym}$/J line (The Jackson Laboratory, RRID: IMSR_JAX:016226). The $Jedi^{fl/fl}$ line was maintained as homozygous. A microglia-specific JKO (mJKO) was generated by crossing the $Jedi^{fl/fl}$ line with the B6.129P2(Cg)-$Cx3cr1^{tm2.1(cre/ERT2)Litt}$/

WganJ line (*Cx3cr1*$^{CreERT2/+}$) (The Jackson Laboratory, RRID: IMSR_JAX:021160). For comparisons involving the mJKO line, littermates with any other combination of the transgenes other than *Cx3cr1*$^{CreERT2/+}$,*Jedi*$^{fl/fl}$ were used as controls. Male and female pups from multiple litters were included in all experiments, and sex was not included as a variable in the analyses.

Primary microglia culture and engulfment assay—P7 littermates were anesthetized in a protective nitrile sleeve on ice for 5–10 min and then decapitated. The cortical tissue was dissected out and roughly chopped with a sterile blade. The tissue was enzymatically dissociated using the Papain Dissociation system according to the manufacturer's instructions (Worthington Biochemical Corporation, Cat#PDS). During the tissue dissection and dissociation steps, T25 flasks were coated for at least 1 h at 37°C with 10 μg/mL poly-D-lysine, then rinsed three times with sterile distilled water and left to airdry in the cell culture hood. Cells were seeded in the T25 flasks (2–4 brains per flask) and grown at 37°C, with 5% CO_2, in media (DMEM/F12+GlutaMAX (Gibco, Cat#10565-018) supplemented with 10% fetal bovine serum and 1% Pen/Strep). Microglia were isolated roughly one week later, when the mixed glia culture reached confluency. To harvest microglia, the flasks were secured in a secondary container and placed in a 37°C shaker for 5 h, shaking at 175rpm. The media, now containing microglia, was transferred into a new tube and centrifuged at 70 x g for 5 min. Except for 100uL of media, the supernatant was pipetted off by hand. Microglia yields from these preparations are small, and the cell pellet was not always readily visible, hence the retention of 100uL of the supernatant. The microglia were resuspended in 1mL of media, and 250uL of the cell suspension was deposited in each chamber of a 4-well chamber slide. The bead engulfment assay was performed the following day with FluoSpheres Carboxylate-modified microspheres (Invitrogen, Cat#F8826). The beads are two microns in diameter, and thus, are too large to be efficiently engulfed via non-specific, non-receptor-mediated endocytic pathways (i.e., fluid-phase endocytosis, also called pinocytosis).[74] The beads were vortexed for 1 min, then diluted 1:33 in 0.5% bovine serum albumin (BSA). This was then further diluted 1:30 in media, yielding the "bead working stock". The media in the 4-well chamber slide was pipetted off by hand and replaced with the bead working stock, taking care to triturate the bead working stock several times between chambers. The microglia were incubated with the beads at 37°C for 4 h, 2 h, and 5 min (0-h time point), in that order: First, the beads were added to the 4-h time point chamber; 2 h later, beads were added to the 2-h time point chamber, and finally, 5 min before endpoint collection, beads were added to the 0-h time point chamber. At endpoint collection, the bead working stock was pipetted off, and the cells were gently rinsed with 1x PBS. Cells were fixed in 10% neutral buffered formalin (NBF) for 10 min at room temperature, then rinsed three times in 1x PBS. Cells were permeabilized for 3 min at room temperature using 0.2% Triton X-100 in 1x PBS, then washed again in 1x PBS. The cells were incubated in blocking solution (5% BSA, 0.1% Tween 20 in 1x PBS) for 15 min at room temperature. Phalloidin-488 methanolic stock (Invitrogen, Cat #A12379) was diluted 1:40 in 1x PBS, and the cells were incubated with the phalloidin-488 working solution for 60 min at room temperature in the dark. Cells were washed for a final time, and the chambers were removed from the slide. The slide was then counterstained with ProLong

Gold with DAPI (Invitrogen, Cat#P36931), and a glass coverslip was placed on top. The slide was left at room temperature in the dark until imaging.

METHOD DETAILS

EdU injections—Reconstituted EdU(5-ethynyl-20-deoxyuridine) stock solution (5 mg/mL in DMSO) was diluted in sterile 1x PBS to make a working solution of 1.25 mg/mL. P7 pups were weighed to calculate the volume necessary to achieve a dose of 15 mg/kg. Due to the low volumes, the volume of EdU working solution that was delivered to the pups were approximate (e.g., if the required volume was 52uL, then the syringe was loaded with ~50uL; if the required volume was 58uL, then the syringe was loaded with ~60uL). Pups were injected subcutaneously in the skin fold on the back of the neck with a 300uL 29G1/2 syringe (Comfort Point, Cat#26018). Pups were injected 30 min apart to allow time for anesthesia, perfusion, and brain removal after the EdU pulse was done. The pups were euthanized 1 h after EdU injection.

Tamoxifen injections—100mg of Tamoxifen (Sigma-Aldrich, Cat#T5648-1G) was resuspended in 1mL pure ethanol and 9mL peanut oil (Sigma-Aldrich, Cat #P2144-250ML). It was administered to dams twice daily starting when the pups were P1 until they were P3. Intraperitoneal injections (100ul, delivering 1mg Tamoxifen) were performed immediately rostral to the inguinal white adipose tissue, alternating sides between injections. To assess *Jedi* transcript levels, RNA was extracted from immunoselected microglia using the RNeasy Micro Kit according to the manufacturer’s instructions (Qiagen, Cat#74004) and quantified on a NanoDrop 2000 (ThermoFisher Scientific, Cat#ND-2000). cDNA was prepared from 50ng of RNA using the SuperScript III First-Strand synthesis system (Invitrogen, Cat#18080051). Quantitative PCR for *Jedi* and *Gapdh* was performed using Sso Universal SYBR Green Supermix (BioRad, Cat#1725271) on the CFX Connect Real-Time System (BioRad, Cat#1855201). The primers are listed in the key resources table.

Tissue processing—To collect tissue for paraffin-embedding, animals were anesthetized in a protective nitrile sleeve on ice for 5–10 min, and then transcardially perfused with 10mL of 1x PBS followed by 10mL of 10% NBF. The solutions were cold and were delivered manually through a syringe and butterfly needle at a flow rate of approximately 1 mL/min. Once the perfusion was complete, the animal was decapitated, and the brain was dissected from the cranium. The brains were post-fixed overnight, each in a separate 15mL tube containing 10% NBF at room temperature. The following day, the brains were washed three times for 20 min in 1x PBS, then secured in cassettes, submerged in containers filled with 70% ethanol, and delivered to the Tissue Pathology Shared Resource of Vanderbilt University Medical Center for embedding. Sections (7-microns-thick) were collected using a sliding microtome and slides were stored at room temperature until staining. To collect tissue for frozen samples, transcardial perfusion and post-fixation were performed as described above, but 4% paraformaldehyde (PFA) was used for both steps instead of NBF. The following day, the brains were cryoprotected by passing through three sucrose solutions of increasing concentration (10%, 20%, and finally, 30%). These steps took place at room temperature. Samples were transferred from one solution to the next only when the tissue had dropped to the bottom of the tube. Once cryoprotected, the brains were embedded in

Optimal Cutting Temperature medium in cryomolds, taking care to document the orientation of the brain in the cryomold to facilitate cryosectioning. Sections (10-micron-thick) were collected on slides and stored at −80°C. Alternatively, 50-μm-thick sections were collected and stored at 4°C in 1x PBS in a 24-well plate sealed with Parafilm.

Immunofluorescent labeling—Apart from experiments that involved staining for Jedi or that used free-floating sections, the following information is applicable to all staining of slide-mounted tissue sections (both paraffin-embedded and frozen): Blocking and antibody incubations were done one the slides (sections were circled with a hydrophobic barrier pen) and in a humidified chamber (a staining tray with a lid and wet paper towels on the bottom of the tray); antigen retrieval/permeabilization and washes were done in plastic Coplin jars; primary antibody incubations were done overnight at 4°C; blocking was done at room temperature for 1 h in blocking solution (5% BSA, 0.1% Tween 20 in 1x PBS); secondary antibodies were diluted 1:1000 in 1x PBS and incubated with the sections for 1 h at room temperature in the dark; washes were performed in sets of three 3-min washes in wash buffer (0.05% Tween 20 in 1x PBS) at room temperature on a rocker; excess liquid was removed by gently tapping the slide on a paper town and/or with a pipette tip connected to the vacuum line; all slides were mounted with a drop of ProLong Gold with DAPI mounting media and a glass coverslip, and left to dry in the dark at room temperature until imaging. For P7 brain sections, we found that ~30uL of solution (e.g., blocking solution, antibodies, etc.) was more than enough to completely cover the section. The diluents and dilutions of primary antibodies varied according to the requirements of the sample and staining techniques and will be indicated below.

To perform immunolabeling on paraffin-embedded samples, the slides were baked at 65°C for 30 min before deparaffinization. Deparaffinization consisted of serial 5-min incubations: three times in xylenes (fresh each time), twice in 100% ethanol (fresh each time), and once in each of the following: 95%, 80%, 70%, and 50% ethanol. The slides were rinsed for 10 min in running distilled water and rinsed in 1x PBS before antigen retrieval. Antigen retrieval was performed in a pressure cooker (such as the Instant Pot) for 15 min using the “manual” mode. Citrate buffer pH 6.0 (0.01M anhydrous citric acid, 0.05% Tween 20, in distilled water) was used for antigen retrieval for IBA1, and Tris-EDTA pH 9.0 (0.01M Tris Base, 1.26mM EDTA, 0.05% Tween 20, in distilled water) was used for MASH1. Importantly, the Coplin jar’s lid was placed on top of the jar but not tightened; it was secured only with several pieces of laboratory tape. After antigen retrieval and before blocking, the slides were rinsed once with 1x PBS. After blocking, the primary antibodies were applied. For paraffin sections, the following primary antibodies were used (with specific diluents and dilutions): Polyclonal Rabbit anti-Mouse IBA1 (FUJIFILM Wako Shibayagi, Cat#019–19741; RRID: AB_839504; used at 1:750 in 1x PBS); Monoclonal Mouse anti-Rat MASH1 (BD Biosciences, clone 24B72D11.1; Cat#556604; RRID: AB_396479; used at 1:200 in blocking solution). After the primary antibody, the slides were washed, and the secondary antibodies were applied. The following secondary antibodies were used: Goat anti-Rabbit 488 (Invitrogen, Cat #A-11008), Donkey anti-Mouse 488 (Invitrogen, Cat #A-21202). The slides were then washed and mounted.

For frozen sections mounted on slides, the slides were removed from the −80°C freezer, placed in a Coplin jar, and post-fixed at room temperature in 4% PFA for 30 min. The slides were rinsed once for 5 min in 1x PBS before permeabilization (0.2% Triton X-100 for 10 min at room temperature). The slides were rinsed again in 1x PBS before blocking. After blocking, the primary antibodies were applied. For frozen sections, the following primary antibodies were used (with specific diluents and dilutions): Polyclonal Sheep anti-Mouse PEAR1 (R&D Systems, Cat#AF7607; RRID: AB_2943660; used at 1:50 in blocking solution); Polyclonal Rabbit anti-Mouse IBA1 (same as for paraffin section but used at 1:500 in blocking solution); Monoclonal Rat anti-Mouse CD68 (Bio-Rad, Cat#MCA1957; RRID: AB_322219; used at 1:100 in blocking solution). After the primary antibody, the slides were washed, and the secondary antibodies were applied. The following secondary antibodies were used: Donkey anti-Rabbit 488 (Invitrogen, Cat#A-21206; used at 1:1000 in blocking solution); Goat anti-Rabbit 647 (Invitrogen, Cat#21245; used at 1:1000 in blocking solution). The slides were then washed and mounted.

The staining protocol was modified for 50-μm-thick free-floating sections: The staining was performed entirely in the wells of 24-well plates. Each well contained two sections, and the sections were transferred between the wells using fine-tipped paintbrushes. Post-fixation was for 1 h at room temperature in 4% PFA followed by a 5-min wash in 1x PBS; the blocking solution used was 5% BSA, 0.3% Triton X-100 in 1x PBS; primary antibody incubation was 48–72 h at 4°C; secondary antibody incubation was 2 h at room temperature in the dark. The aforementioned anti-IBA1 primary antibody was used at the same concentration and in the same diluent as for frozen slide-mounted sections. The secondary used was the Donkey anti-Rabbit 594 (Invitrogen, Cat#A-21207). For mounting, the sections were transferred from the wells to a small pool of 1x PBS on the slide. Paintbrushes were used to position, re-position, and hold the sections in place while a small piece of paper towel was used to wick away the excess liquid until the sections were immobilized on the slide. The slide was left to dry for 5 min before mounting.

The staining protocol for Jedi had several crucial modifications and took place over three days: On day 1, the slides were post-fixed, rinsed, permeabilized, rinse, and blocked as described above. Then, the slides were subjected to two 15-min incubations, first with a Streptavidin blocking solution, and then with a Biotin blocking solution from the Avidin/Biotin Blocking Kit (Vector Laboratories, Cat#SP-2001), each followed by a rinse in 1x PBS. The primary antibody incubation was performed as usual. On day 2, the slides were washed before the secondary antibodies were added. Importantly, all wash steps consisted of three 45-min washes. The secondary antibody incubation was overnight at 4°C. The secondary antibody used to detect Jedi was the Polyclonal Donkey anti-Sheep IgG H&L biotin-conjugated secondary antibody (Invitrogen, Cat#A16045; RRID: AB_2534719; used at 1:1000 in blocking solution (5% BSA, 0.1% Tween 20 in 1x PBS)). On day 3, the slides were washed (three 45-min washes) and incubated with Cy3-Streptavidin (Jackson ImmunoResearch Laboratories, Cat#016-160-084; RRID: AB_2337244) for 1 h at room temperature. The slides were then washed and mounted.

EdU labeling—EdU labeling was performed either alone or following immunolabeling. Sections were incubated with the EdU labeling solution for 30 min at room temperature in the dark and in a humidified chamber, then washed three times for 3 min, and mounted with ProLong Gold with DAPI. EdU labeling solution (for 1mL) was composed of 40uL of 100mM $CuSO_4$ (250mg $CuSO_4$ in 10mL 1x TBS), 1uL of 2mM Sulto-Cynine3 azide (Lumiprobe, Cat#D1330), 100uL of 1M Ascorbic acid sodium salt (20 mg NaAcs (MP Biomedicals, Cat#102890) in 100uL 1X TBS), and 860uL 1x TBS.

TdT-mediated dUTP-X nick end labeling (TUNEL)—The TUNEL assay was performed on sections prior to immunolabeling, according to the manufacturer's instructions but with extended incubation periods (ApopTag Fluorescein *In Situ* Apoptosis Detection Kit, Millipore-Sigma, Cat#S7110). The labeling was performed on paraffin sections, slide-mounted frozen sections, and free-floating frozen sections. For slide-mounted sections, post-fixation and washes were done in plastic Coplin jars, and the tissue was circled with a hydrophobic barrier pen prior to the assay. For floating sections, the assay was done in a 24-well plate. Sections were post-fixed for 10 min at room temperature in 2:1 ethanol: acetic acid, then washed twice for 10 min with 1x PBS. After post-fixation, the free-floating sections sit on top of the 1x PBS, so it is important to gently submerge the sections with a paintbrush. Equilibration Buffer was applied to the sections for 3 min followed by the working strength TdT enzyme for 1.5 h at 37°C in the dark and in a humidified chamber. Following the TdT enzyme incubation, Stop/Wash Buffer was applied and incubated at room temperature for 15 min, then the sections were washed three times for 3 min 1x PBS. Working strength anti-digoxigenin conjugate was applied to the sections for 1 h at room temperature. Sections were then washed three times for 3 min. Immunolabeling was then performed as described above.

V-SVZ microdissection—The ventricular-subventricular zone (V-SVZ) was collected from P7 pups according to regional delineations established previously, specifically regions ii/iiiC and ii/iiiD.[75] Pups were anesthetized in a protective nitrile sleeve on ice for 5–10 min and then decapitated. The brain was dissected out and placed in an empty 10cm dish. The brain was stabilized with one hand using a pair of blunt-tipped curved forceps, and in the other hand, a chilled, sterile straight razor blade was used to cut two to three slices (each 1-2mm-thick) that contained the V-SVZ. The cuts were made in the coronal plane, starting at roughly 3mm caudal to the point at which the dorsal surface of the olfactory bulb meets the most rostral pole of the cortex. The slices were transferred to another 10cm dish under the dissecting scope and laid down on one of the cut surfaces. Several drops of chilled sterile 1x PBS were put on the slices. Using a microscalpel, three cuts were made in a triangle around the dorsal V-SVZ ("the wedge"). This was done on each hemisphere of each slice. The samples were then placed in a 1.5mL tube on ice.

Cytokine analysis—The V-SVZ was collected as described above. Each sample contained tissue pooled from 3 to 6 pups. Tissue was weighed to determine the appropriate volume of lysis buffer (20mM Tris-HCl, 250mM NaCl, 0.05% Tween 20, complete Mini Protease Inhibitor Cocktail EASYpacks tablet (1 tablet for 10mL of lysis buffer) (Roche, Cat#04693124001)) and manually homogenized, then centrifuged at 14K x g for 10 min at 4°C. The supernatant was removed into a new tube and stored at −80°C until analysis. Analysis was performed using the Milliplex Mouse Cytokine Magnetic Kit (EMD Millipore, Cat#MCYTOMAG-70K) and Luminex MAGPIX instrument at the Vanderbilt Hormone Assay and Analytical Service Core. The lysis buffer was used as the matrix solution in the background, standard curve, and control wells.

Immunoselection of microglia—V-SVZ samples were prepared as described above. For RNA sequencing in WT and JKO animals, V-SVZ and cortical tissue were collected and placed in separate tubes. For qPCR of *Jedi* in mJKO and control littermates, only V-SVZ tissue was collected. The samples were dissociated using the Papain Dissociation, and microglia were then isolated from the cell suspension by Magnetic Activated Cell Sorting using anti-Cd11b microbeads according to the manufacturer's instructions, using MS columns and a MiniMACs separator (Miltenyi Biotec, Cat#130-093-634).

RNA sequencing—RNA was isolated as described in the section on tamoxifen injections. RNA was submitted to Vanderbilt University Medical Center VANTAGE Core for poly-A enrichment-based library preparation and sequencing on the Illumina NovaSeq (PE-100). Pre-processed reads were aligned to the mouse genome (mm10, downloaded from UCSC) using TopHat (v2.0.11),[76] and differential gene expression was determined using DESeq2 (v. 1.34.0) as previously described.[70] "Sequencing run" was included in the DESeq assay design to control for batch effect. Genes were considered differentially expressed if they had an adjusted p value <0.05 and a fold change $\geq |1.5|$. Differentially expressed genes were used for gene ontology analysis using clusterProfiler (v. 4.2.2).[71]

It is important to note that one of our cell populations of interest (DIMs) has been suggested to be circulating monocytes that accumulate in the brain over time.[5,77,78] However, in our dataset, monocyte/macrophage-, neutrophil-, or NK cell-associated genes, which were previously identified by single-cell RNA sequencing of $CD11b^+$ sorted microglia,[9] were not differentially expressed in JKO V-SVZ microglia.

Liquid chromatography-mass spectrometry—Samples were collected from the V-SVZ of P7 WT and JKO pups, snap frozen in liquid nitrogen, and stored at −80°C until LC-MS analysis. HPLC-grade methanol, acetonitrile, isopropanol, and formic acid used for sample purification and LC-MS/MS analysis were JT Baker-brand (ThermoFisher Scientific, Waltham, MA). Authentic lipid standards of 6-keto-$PGF_{1\alpha}$, PGE_2, PGD_2, $PGF_{2\alpha}$, PGJ_2, 15-hydroxyeicosanoic acid (15-HETE), 2-arachidonoylglycerol (2-AG), anandamide (AEA), arachidonic acid (AA), oloeylglycerol (OG), and oleoylethanolamide (OEA) were purchased from Cayman Chemicals (Ann Arbor, MI). 16:0 lysophosphatidylcholine (LPC) and 17:0 LPC were purchased from Avanti Polar Lipids (Alabster, AL). The following deuterated internal standards were purchased from Cayman: 6-keto-$PGF_{1\alpha}$-d4, $PGF_{2\alpha}$-d4, PGE_2-d4, PGD_2-d4, PGJ_2-d4, 15-HETE-d8, 2-AG-d5, AEA-d4, AA-d8, and OEA-d4. OG-d5 was purchased from US Biological (Salem, MA). All LC-MS/MS analysis was performed on a Shimadzu Nexera system in-line with an SCIEX 6500 QTrap; except the LPC analysis, which was performed on a Shimadzu LC system in-line with an SCIEX 3200 QTrap mass spectrometer. The 6500 QTrap was equipped with a TurboV Ionspray source and operated in positive and negative ion modes. The 3200 QTrap was equipped with an ionspray source and operated in positive ion mode. For both LC-MS systems, SCIEX Analyst software (ver 1.6.2) was used to control the instruments and acquire and process the data.

Vials containing the brain samples were removed from −80°C storage and placed on dry ice. 0.5 mL of methanolic homogenization solution containing the deuterated internal standards was added to each vial and the vial was sonicated in a bath sonicator filled with ice water. After about 1 min of sonication, the samples were pulverized completely. The samples were then transferred to glass test tubes and centrifuged at ~3,000 rcf for 10 min at 4°C. Roughly 0.4 mL of the supernatant was removed to clean test tubes and evaporated to dryness under nitrogen and either reconstituted for LC-MS analysis or capped and stored at −20°C for later analysis.

Immediately prior to LC-MS analysis, the samples were reconstituted in 70μL MeOH and 40μL H_2O, vortexed, and transferred to autosampler vials. The samples were analyzed on the above-referenced LC-MS systems. For LPC analysis, the analytes were chromatographed on an Phenomenex C18 column (5.0 × 0.21 cm; 3.0 μm) which was held at 43°C. A gradient elution profile was applied to each sample, specifically; an initial hold for 0.30 min followed by an increase in %B from 15% (initial conditions) to 90% over 5.0 min, and a hold at 90% for 0.5 min. The column was subsequently returned to initial conditions for 1.5 min prior to the next injection. The flow rate was 300 μL/minute and component A was 1:1 methanol:water with 5mM ammonium acetate and 0.1% formic acid while component B was 2:1:1 isopropanol:acetonitrile:methanol with 5 mM ammonium acetate and 0.1% formic acid. For all other lipids, the analytes were chromatographed on an Acquity UPLC BEH C18 reversed-phase column (5.0 × 0.21 cm; 1.7 μm) which was held at 43°C. A gradient elution profile was applied to each sample, specifically; an initial hold for 0.25 min followed by an increase in %B from 35% (initial conditions) to 99% over 4.00 min, and a hold at 99% for 0.8 min. Then the column was returned to initial conditions for 1.2 min prior to the next injection. The flow rate was 330 μL/minute and component A was water with 0.05% formic acid while component B was 3:1 acetonitrile:methanol with 0.1% formic acid. All analytes were detected via selected reaction monitoring (SRM) in both negative and positive ion mode. The SRM transition (m/z), collision energy (C.E. - volts) and polarity are given for each analyte in the table below. Italicized values in parentheses indicate that value for the deuterated internal standard. Analytes were quantitated by stable isotope dilution against their deuterated internal standard, except 16:0 LPC, which was quantitated against 17:0 LPC. Data were normalized to grams of tissue.

Intracerebral injections of interleukin-1 receptor antagonist (IL-1RA)—

Intracerebral injections were performed using custom-made clay head molds as described previously.[79] To make the head molds, pups aged P4 and weighing 3 g were euthanized via hypothermia followed by a lethal overdose of 100uL of 2.5% Avertin. Euthanized animals were placed in 3% agarose such that only the head and shoulders were submerged, and the agarose was left to solidify. The pups were carefully removed from the agarose, and the cavity left behind was filled with dental repair resin and allowed to cure for 24–72 h at room temperature in a well-ventilated area. The resin casts were used as models around which to mold Crayola Air-Dry modeling clay; the cast was placed such that the dorsal aspect of the head was oriented up and was visible. The clay was allowed to harden, and the mold was affixed to the top of an inverted Petri dish for stability once under the custom-built injecting rig (kindly provided by Dr. Ihrie).

On the day of the injections, JKO pups aged P4 were weighed to confirm a weight 3 g. Pups were placed in a protective nitrile sleeve, anesthetized on ice for 5–10 min, and then immobilized in the clay head molds using tape; the skin covering the cranium was held taut by transparent tape. A beveled glass needle was pre-loaded with mineral oil and the recombinant human IL-1 receptor inhibitor (IL-1RA, R&D Systems, Cat #280-RA, resuspended in 0.1% BSA), then positioned in the injecting rig at a 90° angle relative to the horizontal plane of the Petri dish and head mold. The needle was centered along the midline between the eyes and the position was calibrated as (x = 0mm, y = 0mm, z = 0mm); the injection site was 3mm caudal and 0.5mm lateral to that starting site, and 3mm down into the brain parenchyma. Pups received 1uL of 1ug/uL IL-1RA or vehicle (0.1% BSA) at these coordinates in the right hemisphere only. To differentiate between the pups that had already received an injection, prior to arousal from anesthesia, the paw was tattooed; each pup had a different combination of tattoos on their fore and rear paws and tail. The pups were placed on a Deltaphase isothermal pad and observed until the suckling and righting reflexes returned, then they were placed in the home cage with the dam and littermates. Pups were observed daily for the next three days for abnormalities. At P7, EdU was administered 1 h prior to euthanasia and processing as described above.

Microscopy—Paraffin sections and 10-μm -thick frozen sections were imaged using a Nikon Eclipse Ti widefield fluorescence microscope with Nikon Plan Fluor 20× (NA: 0.5) or 40× (Oil, NA: 1.3) lenses. An X-Cite 120 LED (Excelitas Technologies) was used. The 50-μm-thick sections and *in vitro* bead engulfment assay were imaged at the Vanderbilt University Cell Imaging Shared Resource using a Zeiss LSM 880 confocal laser scanning microscope. The excitation wavelengths used were 405nm, 488, 561, and 633. The objective lens used was 40x/1.30 C Plan-Apochromat Oil, WD = 0.22mm. For the *in vivo* engulfment analysis using TUNEL and IBA1 co-labeling, the z-step size/voxel depth was 0.427um. For the bead engulfment assay, the z-step size/voxel depth was 0.3um. Image analysis and quantification was performed in FIJI (v1.54f).

QUANTIFICATION AND STATISTICAL ANALYSIS

Statistical analyses were performed using GraphPad Prism 10.0.2 (September 2023). Both one- and two-tailed t tests are used. One-tailed tests were selected when the hypotheses were directional (e.g., Alternative hypothesis (H_1): The number of TUNEL$^+$ cells *is higher* in the V-SVZ of JKO vs. WT. Null hypothesis (H_0): The number of TUNEL$^+$ cells *is not higher* in V-SVZ of JKO vs. WT.) Two-tailed tests were used when the hypothesis was that the measure would be different between groups, but the direction of the change could not be hypothesized (e.g., Alternative hypothesis (H_1): The number of TUNEL$^+$ cells in the cortex and striatum *is different* in JKO vs. WT. Null hypothesis (H_0): The number of TUNEL$^+$ cells in the cortex and striatum *is not different* in JKO vs. WT.) In some cases, the distribution of the data points prompted the use of the Shapiro-Wilk normality test. If the test indicated non-normality, a Mann-Whitney U test was used. If the groups displayed differing variance, then a Welch's t test was used. In all figures, the groups that were tested and the exact p values can be found in the plots. All other statistical information can be found in Table S1. Descriptive statistics will be supplied upon request. The boxplots show the minimum and maximum values, and the 25th, 50th, and 75th percentiles of the data.

In immunofluorescence experiments, each animal was represented by 2–4 slides depending on sample availability, each of which carried 2-4 sections taken from different points along the rostral-caudal axis. During sectioning, the start of sample collection was based on the appearance of gross anatomical features in the sections; the earliest sections, those at the most rostral end of the region of interest, were taken from the point at which the corpus callosum connected and fully traversed the midline. From this point, a minimum of thirty sections were collected across a minimum of ten slides. Depending on how many sections were lost during this process, sectioning usually concluded prior to the appearance of the third ventricle. These regions correspond to ii/iii, as described by Merkle et al.[75] The slides were all numbered in ascending order.

For a given experiment, the slides that were chosen for the staining corresponded to roughly the same points along the rostral-caudal axis between animals, and this was determined not only by the slide number but also by visual inspection of the sections. For example, each animal would contribute slides 1, 5, and 10 to the experiment. Deviations from this would only occur if, upon visual inspection of the sections, one of the slides was found to have sections that were physically damaged (i.e., a rip in the tissue) or if the sections' location in the brain did not closely resemble those of the other animals.

Following selection and prior to staining, the slides were randomized. At each wash step, the slides were once again randomized to avoid their position impacting the outcome measures (e.g., drying out, receiving the last of the antibody solution, etc.). Finally, immediately prior to imaging, the slides were again randomized and numbered (starting at 1) by an individual other than the experimenter who would image the slides. Images of the region of interest were taken from both hemispheres. When the region of interest was located, the image would be captured, even if there was a fold in the tissue, some sort of debris in the field of view, or if the section appeared further rostral or further caudal than what had been expected. These issues were taken into consideration in the next step of the experiment.

Data from immunofluorescent labeling were collected in regions of interest (ROIs) in the dorsal V-SVZ, cortex, and striatum. ROIs were determined with only the DAPI channel visible, which avoids ROI selection bias. In the V-SVZ, the ROI was traced by hand using the regions of dense, bright DAPI signal as a guide. The ependymal lining of the lateral ventricles and the choroid plexus were excluded from the ROIs on account of high autofluorescence and non-specific staining. For analyses in the cortex, the images were centered on the S1 region and excluded the corpus callosum, layer I of the cortex, and the meninges. Similarly, images used for analysis of striatal tissue excluded neighboring structures like the corpus callosum and the V-SVZ. The striatum was analyzed in the same way, and neighboring structures were not in the field of view.

Image processing constituted changes mainly to brightness and, to a lesser extent, contrast of the images and was performed largely by the experimenter, without the use of automated thresholding algorithms, except in the case of EdU quantification. Image processing was limited to two steps: 1) prior to quantification, when determining whether an image met the inclusion criteria (i.e., correct region of interest, absence of artifacts, high enough signal-to-noise ratio to allow quantification), and 2) after quantification and analysis were complete and representative images were selected for the figures; these images were chosen based on whether the number of cells in the ROI represented the mean of the group. Note that Figures 1 and 2 in the main text and Figure S1 use the “Fire” LUT in Fiji to better visualize Jedi even in cases of weak signal without relying on changes in brightness and contrast. The “Fire” LUT translates pixel intensity into different colors, creating a heatmap effect that increases contrast between differing pixel intensities and facilitates the differentiation between real signal and background, even in cases of low signal.

For cell counting, the area outside the ROI was removed using the “Clear outside” command in the “Edit” dropdown menu of FIJI. Our analyses were limited to the dorsal V-SVZ because, in coronal sections, the area of the ventral V-SVZ is very small and presents the challenge of under-sampling. For the quantification of Jedi$^+$ microglia in WT P7 V-SVZ, IBA1$^+$ microglia were counted using “Cell Counter”, and if a cell’s marker co-localized with Jedi staining, then it was marked as a double-labeled cell; the possibility that the Jedi staining corresponded to vascular expression of the protein was ruled out by examining the shape of the Jedi$^+$ area and the nucleus (and neighboring nuclei); vascular/perivascular cells have dense, elongated nuclei with no visible chromatin bodies. Jedi staining does not fill the cell but is instead localized mainly to the processes, so in the absence of Jedi staining in the microglia cell body, the co-localization of Jedi with several IBA1$^+$ processes was enough for the cell to be considered double-positive. For EdU quantification, images were thresholded using the “Moments” algorithm that is available in FIJI. The cells were counted using the “Analyze Particle” function with a range of particle size between 13 and 90 μm^2. The “Analyze Particle” window provides the option to generate a new “mask” image that indicates the cells that were counted. The LUTs of the original thresholded image and the mask were changed to red and green, respectively, and upon merging the two images, any remaining EdU$^+$ cells that did not meet the particle counter’s criteria (i.e., a clump of EdU cells) would be counted by hand. MASH1 quantification was based on counting nuclei by hand, both those with smooth, uniform staining of the entire nucleus and those with clustered, bright puncta that co-localized with a DAPI$^+$ healthy nucleus (i.e., not condensed). TUNEL$^+$ puncta were scored in a similar way, including large, brightly labeled nuclei; large dimly labeled nuclei; and small brightly labeled puncta that overlapped with DAPI, even if it was not clearly associated with a whole nucleus (e.g., apoptotic bleb). For the 50-µm-thick sections, the experimenter counted TUNEL$^+$ puncta in the same way as just described, in each optical section and then considered the dead cell engulfed if it was found within the IBA1-stained area of a microglia, either in a process (“ball-and-chain” configuration) or in the soma.

To measure IBA1-stained area, background signal was mitigated by-hand by increasing the threshold for minimum pixel intensity such that surrounding neuropil was effectively black, and then the image was thresholded and converted to a binary image. The “Set Measurements” window in the “Analyze” dropdown menu in the FIJI Toolbar gives the option of limiting the area measurement to thresholded area. To quantify microglia cell number and cell shape using 50-µm-thick sections in WT and JKO samples, maximum intensity projections were created from the z stack. For the latter two analyses, the perimeters of fifteen randomly selected microglia were traced and measured, as was the area. The circularity index was defined as $4\pi[\text{area}]/[\text{perimeter}]^2$ by Heindl et al.[33]

Quantification of microglia morphology in control and mJKO samples was done with 10-μm-thick sections, which does not allow the experimenter to visualize the entirety of the cell, so all IBA1$^+$ structures were traced and their areas measured. IBA1$^+$ structures with an area of less than 100 μm^2 were considered processes belonging to a microglia cell that was outside the section, and so, were excluded from the analysis.

For the bead engulfment assay, the values collected for this assay allowed the calculation of the percentage of cells performing engulfment and the phagocytic index, defined as (the number of engulfed beads/the total number of cells) x (the number of engulfing/the total number of cells) x 100. The phagocytic index provides a score that combines an approximate measure of "engulfed beads per cell" and the percentage of microglia performing engulfment. The number of engulfed beads was determined using orthogonal views; a bead was considered engulfed if it was estimated that more than 90% of the bead surface was found inside the engulfing cell.

During data collection, the experimenter was blinded to the genotype and treatment group of the samples until all the raw data were collected and recorded. Traced ROIs and.tif files of analyzed images (e.g., counter windows) were saved for future use, if needed.

Supplementary Material

Refer to Web version on PubMed Central for supplementary material.

ACKNOWLEDGMENTS

We thank M. Tugend and F.E. Hickman for their work at the early stage of the project, C. Nelson and K. Volk for their organizational support and technical guidance, and A. Sierra for her thoughtful discussions and guidance. Research in the Ihrie lab is supported by the National Institutes of Health (R01NS118580), the Ben & Catherine Ivy Foundation, and a gift from the Michael David Greene Brain Cancer Fund at the Vanderbilt-Ingram Cancer Center. Research in the Maguire-Zeiss lab is supported by the National Institute of Neurological Disorders and Stroke (R01NS083410). Research in the Carter lab is supported by the National Institute of Neurological Disorders and Stroke (R01NS102365). V.M. has received funding from the National Institutes of Health (5T32DK007563-33) and the National Institute of Child Health and Human Development (7F32HD107930-02).

REFERENCES

1. Anderson SR, and Vetter ML (2019). Developmental roles of microglia: A window into mechanisms of disease. Dev. Dyn 248, 98–117. 10.1002/dvdy.1. [PubMed: 30444278]
2. Nugent AA, Lin K, van Lengerich B, Lianoglou S, Przybyla L, Davis SS, Llapashtica C, Wang J, Kim DJ, Xia D, et al. (2020). TREM2 Regulates Microglial Cholesterol Metabolism upon Chronic Phagocytic Challenge. Neuron 105, 837–854.e9. 10.1016/j.neuron.2019.12.007. [PubMed: 31902528]
3. Deczkowska A, Keren-Shaul H, Weiner A, Colonna M, Schwartz M, and Amit I (2018). Disease-Associated Microglia: A Universal Immune Sensor of Neurodegeneration. Cell 173, 1073–1081. 10.1016/j.cell.2018.05.003. [PubMed: 29775591]
4. Keren-Shaul H, Spinrad A, Weiner A, Matcovitch-Natan O, Dvir-Szternfeld R, Ulland TK, David E, Baruch K, Lara-Astaiso D, Toth B , et al. (2017). A Unique Microglia Type Associated with Restricting Development of Alzheimer's Disease. Cell 160, 1276–1290.e17. 10.1016/j.cell.2017.05.018.
5. Silvin A, Uderhardt S, Piot C, Da Mesquita S, Yang K, Geirsdottir L, Mulder K, Eyal D, Liu Z, Bridlance C, et al. (2022). Dual ontogeny of disease-associated microglia and disease

inflammatory macrophages in aging and neurodegeneration. Immunity 55, 1448–1465.e6. 10.1016/j.immuni.2022.07.004. [PubMed: 35931085]

6. Sierra A, Encinas JM, Deudero JJP, Chancey JH, Enikolopov G, Overstreet-Wadiche LS,Tsirka SE, and Maletic-Savatic M (2010). Microglia shape adult hippocampal neurogenesis through apoptosis-coupled phagocytosis. Cell Stem Cell 7, 483–495. 10.1016/j.stem.2010.08.014. [PubMed: 20887954]
7. Diaz-Aparicio I, Paris I, Sierra-Torre V, Plaza-Zabala A, Rodríguez-Iglesias N, Márquez-Ropero M, Beccari S, Huguet P, Abiega O, Alberdi E, et al. (2020). Microglia Actively Remodel Adult Hippocampal Neurogenesis through the Phagocytosis Secretome. J. Neurosci 40, 1453–1482. 10.1523/JNEUROSCI.0993-19.2019. [PubMed: 31896673]
8. Hammond TR, Dufort C, Dissing-Olesen L, Giera S, Young A, Wysoker A,Walker AJ, Gergits F, Segel M, Nemesh J, et al. (2019). Single-Cell RNA Sequencing of Microglia throughout the Mouse Lifespan and in the Injured Brain Reveals Complex Cell-State Changes. Immunity 50, 253–271.e6. 10.1016/j.immuni.2018.11.004. [PubMed: 30471926]
9. Li Q, Cheng Z, Zhou L, Darmanis S, Neff NF, Okamoto J, Gulati G, Bennett ML, Sun LO, Clarke LE, et al. (2019). Developmental Heterogeneity of Microglia and Brain Myeloid Cells Revealed by Deep Single-Cell RNA Sequencing. Neuron 107, 207–223.e10. 10.1016/j.neuron.2018.12.006.
10. Galli R, Gritti A, Bonfanti L, and Vescovi AL (2003). Neural Stem Cells. Circ. Res 92, 598–608. 10.1161/01.RES.0000065580.02404.F4. [PubMed: 12676811]
11. Blaschke AJ, Weiner JA, and Chun J (1998). Programmed cell death is a universal feature of embryonic and postnatal neuroproliferative regions throughout the central nervous system. J. Comp. Neurol 396, 39–50. 10.1002/(SICI)1096-9861(19980622)396:1<39::AID-CNE4>3.0.CO;2-J. [PubMed: 9623886]
12. Mayer M, and Noble M (1994). N-acetyl-L-cysteine is a pluripotent protector against cell death and enhancer of trophic factor-mediated cell survival in vitro. Proc. Natl. Acad. Sci. USA 91, 7496–7500. 10.1073/pnas.91.16.7496. [PubMed: 7914368]
13. Morshead CM, Craig CG, and van der Kooy D (1998). In vivo clonal analyses reveal the properties of endogenous neural stem cell proliferation in the adult mammalian forebrain. Development 125, 2251–2261. 10.1242/dev.125.12.2251. [PubMed: 9584124]
14. Craig CG, D'sa R, Morshead CM, Roach A, and van der Kooy D (1999). Migrational analysis of the constitutively proliferating subependyma population in adult mouse forebrain. Neuroscience 93, 1197–1206. 10.1016/S0306-4522(99)00232-8. [PubMed: 10473285]
15. Alam MJ, Kitamura T, Saitoh Y, Ohkawa N, Kondo T, and Inokuchi K (2018). Adult Neurogenesis Conserves Hippocampal Memory Capacity. J. Neurosci 38, 6854–6863. 10.1523/JNEUROSCI.2976-17.2018. [PubMed: 29986876]
16. Terranova JI, Ogawa SK, and Kitamura T (2019). Adult hippocampal neurogenesis for systems consolidation of memory. Behav. Brain Res 372, 112035. 10.1016/j.bbr.2019.112035. [PubMed: 31201874]
17. Cunningham CL, Martínez-Cerdeño V, and Noctor SC (2013). Microglia Regulate the Number of Neural Precursor Cells in the Developing Cerebral Cortex. J. Neurosci 33, 4216–4233. 10.1523/JNEUROSCI.3441-12.2013. [PubMed: 23467340]
18. Ribeiro Xavier AL, Kress BT, Goldman SA, Lacerda de Menezes JR, and Nedergaard M (2015). A Distinct Population of Microglia Supports Adult Neurogenesis in the Subventricular Zone. J. Neurosci 35, 11848–11861. [PubMed: 26311768]
19. Kreisel T, Wolf B, Keshet E, and Licht T (2019). Unique role for dentate gyrus microglia in neuroblast survival and in VEGF-induced activation. Glia 67, 594–618. 10.1002/glia.23505. [PubMed: 30453385]
20. Fourgeaud L, Través PG, Tufail Y, Leal-Bailey H, Lew ED, Burrola PG, Callaway P, Zagórska A, Rothlin CV, Nimmerjahn A, and Lemke G (2016). TAM receptors regulate multiple features of microglial physiology. Nature 532, 240–244. 10.1038/nature17630. [PubMed: 27049947]
21. Paolicelli RC, Sierra A, Stevens B, Tremblay M-E, Aguzzi A, Ajami B , Amit I, Audinat E, Bechmann I, Bennett M, et al. (2022). Microglia states and nomenclature: A field at its crossroads. Neuron 110, 3458–3483. 10.1016/j.neuron.2022.10.020. [PubMed: 36327895]

22. Yin Z, Rosenzweig N, Kleemann KL, Zhang X, Brandão W, Margeta MA, Schroeder C, Sivanathan KN, Silveira S, Gauthier C, et al. (2023). APOE4 impairs the microglial response in Alzheimer's disease by inducing TGFβ-mediated checkpoints. Nat. Immunol 24, 1839–1853. 10.1038/s41590-023-01627-6. [PubMed: 37749326]
23. Puntambekar SS, Moutinho M, Lin PB-C, Jadhav V, Tumbleson-Brink D, Balaji A, Benito MA, Xu G, Oblak A, Lasagna-Reeves CA, et al. (2022). CX3CR1 deficiency aggravates amyloid driven neuronal pathology and cognitive decline in Alzheimer's disease. Mol. Neurodegener 17, 47. 10.1186/s13024-022-00545-9. [PubMed: 35764973]
24. Butler CA, Popescu AS, Kitchener EJA, Allendorf DH, Puigdellívol M, and Brown GC (2021). Microglial phagocytosis of neurons in neurodegeneration, and its regulation. J. Neurochem 158, 621–639. 10.1111/jnc.15327. [PubMed: 33608912]
25. Marschallinger J, Iram T, Zardeneta M, Lee SE, Lehallier B, Haney MS, Pluvinage JV, Mathur V, Hahn O, Morgens DW, et al. (2020). Lipid-droplet-accumulating microglia represent a dysfunctional and proinflammatory state in the aging brain. Nat. Neurosci 23, 194–208. 10.1038/s41593-019-0566-1. [PubMed: 31959936]
26. Wu H-H, Bellmunt E, Scheib JL, Venegas V, Burkert C, Reichardt LF, Zhou Z, Fariñas I, and Carter BD (2009). Glial precursors clear sensory neuron corpses during development via Jedi-1, an engulfment receptor. Nat. Neurosci 12, 1534–1541. 10.1038/nn.2446. [PubMed: 19915564]
27. Scheib JL, Sullivan CS, and Carter BD (2012). Jedi-1 and MEGF10 Signal Engulfment of Apoptotic Neurons through the Tyrosine Kinase Syk. J. Neurosci 32, 13022–13031. 10.1523/JNEURO-SCI.6350-11.2012. [PubMed: 22993420]
28. Wang S, Sudan R, Peng V, Zhou Y, Du S, Yuede CM, Lei T, Hou J, Cai Z, Cella M, et al. (2022). TREM2 drives microglia response to amyloid-β via SYK-dependent and -independent pathways. Cell 185, 4153–4169.e19. 10.1016/j.cell.2022.09.033. [PubMed: 36306735]
29. Bennett ML, Bennett FC, Liddelow SA, Ajami B, Zamanian JL, Fernhoff NB, Mulinyawe SB, Bohlen CJ, Adil A, Tucker A, et al. (2016). New tools for studying microglia in the mouse and human CNS. Proc. Natl. Acad. Sci. USA 113, E1738–E1746. 10.1073/pnas.1525528113. [PubMed: 26884166]
30. Vandenbriele C, Kauskot A, Vandersmissen I, Criel M, Geenens R, Craps S, Luttun A, Janssens S, Hoylaerts MF, and Verhamme P (2015). Platelet endothelial aggregation receptor-1: a novel modifier of neoangiogenesis. Cardiovasc. Res 108, 124–138. 10.1093/cvr/cvv193. [PubMed: 26156496]
31. Guttenplan KA, Weigel MK, Adler DI, Couthouis J, Liddelow SA, Gitler AD, and Barres BA (2020). Knockout of reactive astrocyte activating factors slows disease progression in an ALS mouse model. Nat. Commun 11, 3753. 10.1038/s41467-020-17514-9. [PubMed: 32719333]
32. Ravichandran KS (2010). Find-me and eat-me signals in apoptotic cell clearance: progress and conundrums. J. Exp. Med 207, 1807–1817. 10.1084/jem.20101157. [PubMed: 20805564]
33. Heindl S, Gesierich B, Benakis C, Llovera G, Duering M, and Liesz A (2018). Automated Morphological Analysis of Microglia After Stroke. Front. Cell. Neurosci 12, 106. 10.3389/fncel.2018.00106. [PubMed: 29725290]
34. Stopper L, Bălşeanu TA, Cătălin B, Rogoveanu OC, Mogoantă L, and Scheller A (2018). Microglia morphology in the physiological and diseased brain - from fixed tissue to in vivo conditions. Rom. J. Morphol. Embryol 59, 7–12. [PubMed: 29940606]
35. Butovsky O, Jedrychowski MP, Moore CS, Cialic R, Lanser AJ, Gabriely G, Koeglsperger T, Dake B, Wu PM, Doykan CE, et al. (2014). Identification of a unique TGF-β-dependent molecular and functional signature in microglia. Nat. Neurosci 17, 131–143. 10.1038/nn.3599. [PubMed: 24316888]
36. Cacci E, Ajmone-Cat MA, Anelli T, Biagioni S, and Minghetti L (2008). In vitro neuronal and glial differentiation from embryonic or adult neural precursor cells are differently affected by chronic or acute activation of microglia. Glia 56, 412–25. 10.1002/glia.20616. [PubMed: 18186084]
37. Gorica E, and Calderone V (2022). Arachidonic Acid Derivatives and Neuroinflammation. CNS Neurol. Disord.: Drug Targets 21, 118–129. 10.2174/1871527320666210208130412. [PubMed: 33557740]

38. Marinelli S, Marrone MC, Di Domenico M, and Marinelli S (2023). Endocannabinoid signaling in microglia. Glia 71, 71–90. 10.1002/glia.24281. [PubMed: 36222019]

39. Xu J, Storer PD, Chavis JA, Racke MK, and Drew PD (2005). Agonists for the peroxisome proliferator-activated receptor-alpha and the retinoid X receptor inhibit inflammatory responses of microglia. J. Neurosci. Res 81, 403–411. 10.1002/jnr.20518. [PubMed: 15968640]

40. Shigemoto-Mogami Y, Hoshikawa K, Goldman JE, Sekino Y, and Sato K (2014). Microglia Enhance Neurogenesis and Oligodendrogenesis in the Early Postnatal Subventricular Zone. J. Neurosci 34, 2231–2243. 10.1523/JNEUROSCI.1619-13.2014. [PubMed: 24501362]

41. Girard S, Sébire H, Brochu M-E, Briota S, Sarret P, and Sébire G (2012). Postnatal administration of IL-1Ra exerts neuroprotective effects following perinatal inflammation and/or hypoxic-ischemic injuries. Brain Behav. Immun 26, 1331–1339. 10.1016/j.bbi.2012.09.001. [PubMed: 22982341]

42. Kaneko N, Kudo K, Mabuchi T, Takemoto K, Fujimaki K, Wati H, Iguchi H, Tezuka H, and Kanba S (2006). Suppression of Cell Proliferation by Interferon-Alpha through Interleukin-1 Production in Adult Rat Dentate Gyrus. Neuropsychopharmacol 31, 2619–2626. 10.1038/sj.npp.1301137.

43. Guadagno J, Swan P, Shaikh R, and Cregan SP (2015). Microglia-derived IL-1β triggers p53-mediated cell cycle arrest and apoptosis in neural precursor cells. Cell Death Dis. 6, e1779. 10.1038/cddis.2015.151. [PubMed: 26043079]

44. Ji R, Tian S, Lu HJ, Lu Q, Zheng Y, Wang X, Ding J, Li Q, and Lu Q (2013). TAM Receptors Affect Adult Brain Neurogenesis by Negative Regulation of Microglial Cell Activation. J. Immunol 191, 6165–6177. 10.4049/jimmunol.1302229. [PubMed: 24244024]

45. Ji R, Meng L, Jiang X, Cvm NK, Ding J, Li Q, and Lu Q (2014). TAM receptors support neural stem cell survival, proliferation and neuronal differentiation. PLoS One 9, e115140. 10.1371/journal.pone.0115140. [PubMed: 25514676]

46. Dixon KO, O'Flynn J, van der Kooij SW, and van Kooten C (2014). Phagocytosis of apoptotic or necrotic cells differentially regulates the transcriptional expression of IL-12 family members in dendritic cells. J. Leukoc. Biol 96, 313–324. 10.1189/jlb.3A1013-538RR. [PubMed: 24782489]

47. Poon IKH, Hulett MD, and Parish CR (2010). Molecular mechanisms of late apoptotic/necrotic cell clearance. Cell Death Differ. 17, 381–397. 10.1038/cdd.2009.195. [PubMed: 20019744]

48. Franc NC, White K, and Ezekowitz RA (1999). Phagocytosis and development: back to the future. Curr. Opin. Immunol 11, 47–52. 10.1016/s0952-7915(99)80009-0. [PubMed: 10047544]

49. Wu MD, Montgomery SL, Rivera-Escalera F, Olschowka JA, and O'Banion MK (2013). Sustained IL-1β expression impairs adult hippocampal neurogenesis independent of IL-1 signaling in nestin+ neural precursor cells. Brain Behav. Immun 32, 9–18. 10.1016/j.bbi.2013.03.003. [PubMed: 23510988]

50. De SR, Ajmone-Cat MA, Nicolini A, and Minghetti L (2002). Expression of Phosphatidylserine Receptor and Down-Regulation of ProInflammatory Molecule Production by its Natural Ligand in Rat Microglial Cultures. J. Neuropathol. Exp. Neurol 61, 237–244. 10.1093/jnen/61.3.237. [PubMed: 11895038]

51. Ajmone-Cat MA, De Simone R, Nicolini A, and Minghetti L (2003). Effects of phosphatidylserine on p38 mitogen activated protein kinase, cyclic AMP responding element binding protein and nuclear factor-kappaB activation in resting and activated microglial cells. J. Neurochem 84, 413–416. 10.1046/j.1471-4159.2003.01562.x. [PubMed: 12559004]

52. De Simone R, Ajmone-Cat MA, Tirassa P, and Minghetti L (2003). Apoptotic PC12 Cells Exposing Phosphatidylserine Promote the Production of Anti-Inflammatory and Neuroprotective Molecules by Microglial Cells. J. Neuropathol. Exp. Neurol 62, 208–216. 10.1093/jnen/62.2.208. [PubMed: 12578230]

53. Minghetti L, Ajmone-Cat MA, De Berardinis MA, and De Simone R (2005). Microglial activation in chronic neurodegenerative diseases: roles of apoptotic neurons and chronic stimulation. Brain Res. Rev 48, 251–256. 10.1016/j.brainresrev.2004.12.015. [PubMed: 15850664]

54. Smyth EM, Grosser T, Wang M, Yu Y, and FitzGerald GA (2009). Prostanoids in health and disease. J. Lipid Res 50, S423–S428. 10.1194/jlr.R800094-JLR200. [PubMed: 19095631]

55. Ampomah PB, Cai B, Sukka SR, Gerlach BD, Yurdagul A, Wang X, Kuriakose G, Darville LNF, Sun Y, Sidoli S, et al. (2022). Macrophages use apoptotic cell-derived methionine and

DNMT3A during efferocytosis to promote tissue resolution. Nat. Metab 4, 444–457. 10.1038/s42255-022-00551-7. [PubMed: 35361955]

56. Mohri I, Taniike M, Taniguchi H, Kanekiyo T, Aritake K, Inui T, Fukumoto N, Eguchi N, Kushi A, Sasai H, et al. (2006). Prostaglandin D2-Mediated Microglia/Astrocyte Interaction Enhances Astrogliosis and Demyelination in twitcher. J. Neurosci 26, 4383–4393. 10.1523/JNEUROSCI.4531-05.2006. [PubMed: 16624958]
57. Zhang J, Fujii S, Wu Z, Hashioka S, Tanaka Y, Shiratsuchi A, Nakanishi Y, and Nakanishi H (2006). Involvement of COX-1 and up-regulated prostaglandin E synthases in phosphatidylserine liposome-induced prostaglandin E2 production by microglia. J. Neuroimmunol 172, 112–120. 10.1016/j.jneuroim.2005.11.008. [PubMed: 16371234]
58. Stock C, Schilling T, Schwab A, and Eder C (2006). Lysophosphatidylcholine Stimulates IL-1β Release from Microglia via a P2X7 Receptor-Independent Mechanism. J. Immunol 177, 8560–8568. 10.4049/jimmunol.177.12.8560. [PubMed: 17142754]
59. Liu-Wu Y, Hurt-Camejo E, and Wiklund O (1998). Lysophosphatidylcholine induces the production of IL-1β by human monocytes. Atherosclerosis 137, 351–357. 10.1016/S0021-9150(97)00295-5. [PubMed: 9622278]
60. Brown GC, and Neher JJ (2014). Microglial phagocytosis of live neurons. Nat. Rev. Neurosci 15, 209–216. 10.1038/nrn3710. [PubMed: 24646669]
61. Neher JJ, Emmrich JV, Fricker M, Mander PK, Théry C, and Brown GC (2013). Phagocytosis executes delayed neuronal death after focal brain ischemia. Proc. Natl. Acad. Sci. USA 110, E4098–E4107. 10.1073/pnas.1308679110. [PubMed: 24101459]
62. Neher JJ, Neniskyte U, Zhao J-W, Bal-Price A, Tolkovsky AM, and Brown GC (2011). Inhibition of microglial phagocytosis is sufficient to prevent inflammatory neuronal death. J. Immunol 186, 4973–4983. 10.4049/jimmunol.1003600. [PubMed: 21402900]
63. Zalocusky KA, Najm R, Taubes AL, Hao Y, Yoon SY, Koutsodendris N, Nelson MR, Rao A, Bennett DA, Bant J, et al. .(2021). Neuronal ApoE upregulates MHC-I expression to drive selective neurodegeneration in Alzheimer's disease. Nat. Neurosci 24, 786–798. 10.1038/s41593-021-00851-3. [PubMed: 33958804]
64. Young KF, Gardner R, Sariana V, Whitman SA, Bartlett MJ, Falk T, and Morrison HW (2021). Can quantifying morphology and TMEM119 expression distinguish between microglia and infiltrating macrophages after ischemic stroke and reperfusion in male and female mice? J. Neuroinflammation 18, 58. 10.1186/s12974-021-02105-2. [PubMed: 33618737]
65. Ruan C, and Elyaman W (2022).A New Understanding of TMEM119 as a Marker of Microglia. Front. Cell. Neurosci 16, 902372. [PubMed: 35769325]
66. Kaiser T, and Feng G (2019). Tmem119-EGFP and Tmem119-CreERT2 Transgenic Mice for Labeling and Manipulating Microglia. eNeuro 6, ENEURO.0448-18.2019. 10.1523/ENEURO.0448-18.2019.
67. Sahasrabuddhe V, and Ghosh HS (2022). Cx3Cr1-Cre induction leads to microglial activation and IFN-1 signaling caused by DNA damage in early postnatal brain. Cell Rep. 38, 110252. 10.1016/j.cel-rep.2021.110252. [PubMed: 35045285]
68. Lee C-M, Zhou L, Liu J, Shi J, Geng Y, Liu M, Wang J, Su X, Barad N, Wang J, et al. (2020). Single-cell RNA-seq analysis revealed long-lasting adverse effects of tamoxifen on neurogenesis in prenatal and adult brains. Proc. Natl. Acad. Sci. USA 117, 19578–19589. 10.1073/pnas.1918883117. [PubMed: 32727894]
69. Trevisan AJ, Bauer MB, Brindley RL, Currie KPM, and Carter BD (2020). Jedi-1 deficiency increases sensory neuron excitability through a non-cell autonomous mechanism. Sci. Rep 10, 1300. 10.1038/s41598-020-57971-2. [PubMed: 31992767]
70. Love MI, Huber W, and Anders S (2014). Moderated estimation of fold change and dispersion for RNA-seq data with DESeq2. Genome Biol. 15, 550. 10.1186/s13059-014-0550-8. [PubMed: 25516281]
71. Yu G, Wang L-G, Han Y, and He Q-Y (2012). clusterProfiler: an R package for comparing biological themes among gene clusters. OMICS 16, 284–287. 10.1089/omi.2011.0118. [PubMed: 22455463]

72. Zalewska A. (2019). Developmental milestones in neonatal and juvenile C57Bl/6 mouse - Indications for the design of juvenile toxicity studies. Reprod. Toxicol 88, 91–128. 10.1016/j.reprotox.2019.07.019. [PubMed: 31386883]
73. Ahern TH, Krug S, Carr AV, Murray EK, Fitzpatrick E, Bengston L, McCutcheon J, De Vries GJ, and Forger NG (2013). Cell Death Atlas of the Postnatal Mouse Ventral Forebrain and Hypothalamus: Effects of Age and Sex. J. Comp. Neurol 521, 2551–2569. 10.1002/cne.23298. [PubMed: 23296992]
74. Swanson JA, and Yoshida S (2016). Macropinocytosis. In Encyclopedia of Cell Biology, Bradshaw RA and Stahl PD, eds. (Academic Press), pp. 758–765. 10.1016/B978-0-12-394447-4.20084-9.
75. Merkle FT, Mirzadeh Z, and Alvarez-Buylla A (2007). Mosaic Organization of Neural Stem Cells in the Adult Brain. Science 317, 381–384. 10.1126/science.1144914. [PubMed: 17615304]
76. Trapnell C, Hendrickson DG, Sauvageau M, Goff L, Rinn JL, and Pachter L (2013). Differential analysis of gene regulation at transcript resolution with RNA-seq. Nat. Biotechnol 31, 46–53. 10.1038/nbt.2450. [PubMed: 23222703]
77. Mizutani M, Pino PA, Saederup N, Charo IF, Ransohoff RM, and Cardona AE (2012). The fractalkine receptor but not CCR2 is present on microglia from embryonic development throughout adulthood. J. Immunol 188, 29–36. 10.4049/jimmunol.1100421. [PubMed: 22079990]
78. Saederup N, Cardona AE, Croft K, Mizutani M, Cotleur AC, Tsou C-L, Ransohoff RM, and Charo IF (2010). Selective Chemokine Receptor Usage by Central Nervous System Myeloid Cells in CCR2-Red Fluorescent Protein Knock-In Mice. PLoS One 5, e13693. 10.1371/journal.pone.0013693. [PubMed: 21060874]
79. Chervonski E, Brockman AA, Khurana R, Chen Y, Greenberg S, Hay MS, Luo Y, Miller J, Patelis D, Whitney SK, et al. (2021). Creation and validation of 3D-printed head molds for stereotaxic injections of neonatal mouse brains. J. Neurosci. Methods 360, 109255. 10.1016/j.jneumeth.2021.109255. [PubMed: 34139267]

Highlights

- *Jedi-1*-null microglia are poor phagocytes and fail to clear apoptotic cells in the brain
- Microglia lacking Jedi-1 adopt a neuroinflammatory phenotype
- Microglia-specific loss of Jedi-1 results in reduced neonatal neurogenesis
- Inhibition of interleukin-1 receptor signaling rescues neurogenesis in *Jedi-1*-null mice

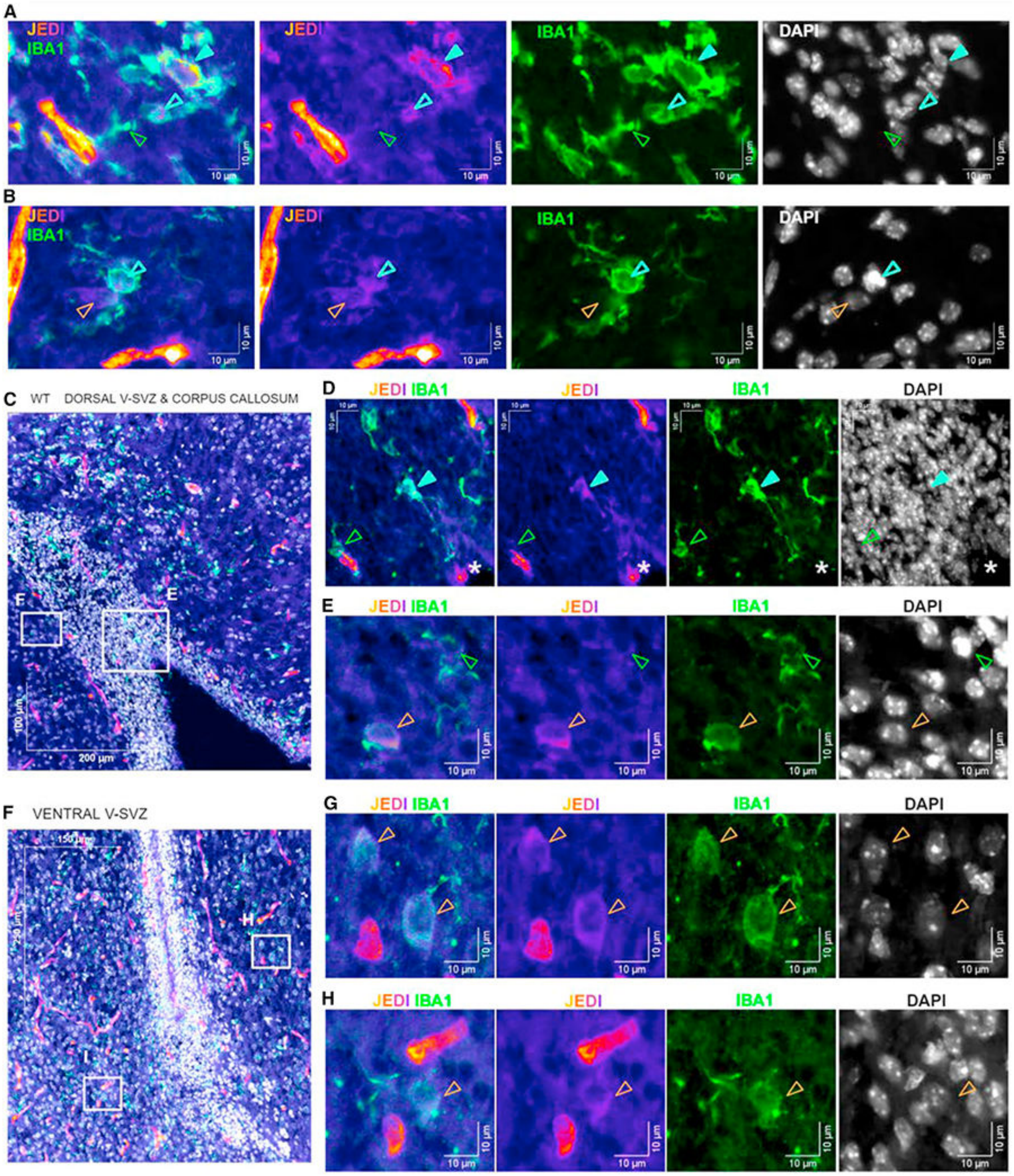

Figure 1. Jedi co-localizes with microglia in the early postnatal V-SVZ and corpus callosum

(A and B) Representative images of Jedi and IBA1 immunofluorescent labeling co-localized in a microglia cell body (closed cyan arrowhead) and phagocytic cups (open cyan arrowheads) in the V-SVZ and corpus callosum of a P7 WT animal. A pyknotic nucleus (bright white circle) co-localizes with a Jedi$^+$IBA1$^+$ phagocytic cup (open cyan arrowhead, B). Some microglia processes have weak to no Jedi signal (open green arrowhead, A). Weak Jedi signal is visible in a cell body that is not clearly IBA1$^+$ (open orange arrowhead). Strong Jedi signal is visible in blood vessels. Scale bars, 10 μm.

(C–E) Image showing the dorsal V-SVZ (C). Scale bar, 200 μm. Images of immunofluorescent labeling of Jedi and IBA1 co-localization (closed cyan arrowhead, D) and IBA1$^+$ microglia processes with low to no Jedi signal (open green arrowheads, D and E) in and bordering the V-SVZ (D and E, respectively, indicated by white boxes in C). Jedi and IBA1 signals co-localize in a process extended toward the surface of the lateral ventricle (asterisk, D). Weak Jedi signal is visible in a cell body that is not clearly IBA1$^+$ (open orange arrowhead, E). Scale bars, 10 μm.

(F–H) Images showing the ventral V-SVZ and adjacent areas (G and H) that correspond with the rostral migratory stream (RMS) (F). Scale bar in (F), 150 μm. Diffuse Jedi signal overlaps with IBA1 staining in large cell bodies in the presumptive RMS (open orange arrowheads), one of which appears to have or is being contacted by an IBA1$^+$ process. Strong Jedi signal is visible in blood vessels. Scale bars, 10 μm.

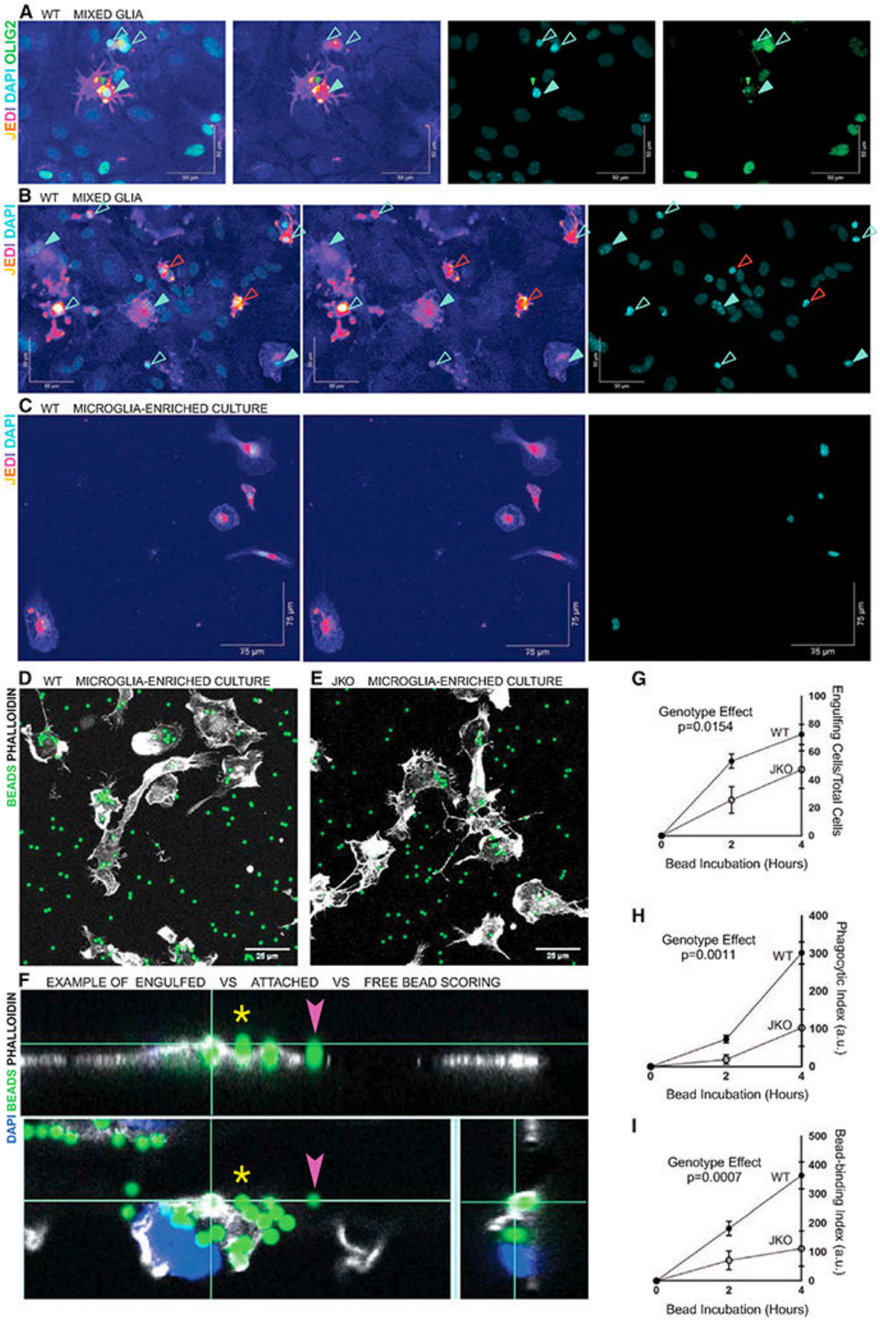

Figure 2. Jedi co-localizes with cultured microglia and contributes to engulfment behavior

(A and B) Representative immunofluorescence images of different Jedi staining patterns in mixed glia cultures from the whole cerebrum of WT P7 animals. Jedi signal co-localizes with microglia cell bodies (closed cyan arrowheads) as well as processes and phagocytic cups associated with pyknotic nuclei (open cyan arrowheads). Strong Jedi signal co-localizes with an OLIG2$^+$ pyknotic nucleus (bright green circle, A) and OLIG2$^+$ puncta near the soma (small green arrowhead, A). Strong Jedi signal surrounds condensed nuclei in the absence of a Jedi$^+$ microglia (open red arrowheads, B). Scale bars, 50 μm.

(C) Representative immunofluorescence image of Jedi staining in microglia-enriched cultures 1 day after isolation. Scale bar, 75 μm.

(D and E) Representative images of WT (D) and JKO (E) microglia-enriched cultures (microglia are white) engulfing beads (green). Scale bars, 25 μm.

(F) Representative optical slice and orthogonal views of z stacks used to score a bead as engulfed (yellow asterisk) or not engulfed (magenta arrowhead).

(G) Quantification of the percentage of WT or JKO microglia performing bead engulfment at three time points from three independent assays (n = 3, error bars = SEM).

(H) Quantification of the phagocytic index ([the number of engulfed beads/the total number of cells] × [the number of engulfing/the total number of cells] × 100), a score that combines an approximate measure of “engulfed beads per cell” and the percentage of microglia performing engulfment. a.u., arbitrary units. From three independent assays (n = 3, error bars = SEM).

(I) Quantification of the bead-binding index (calculated in the same way as the phagocytic index but using the number of “cell-associated (i.e., “bound”), not engulfed beads” instead of “engulfed beads.” a.u., arbitrary units. From three independent assays (n = 3, error bars = SEM).

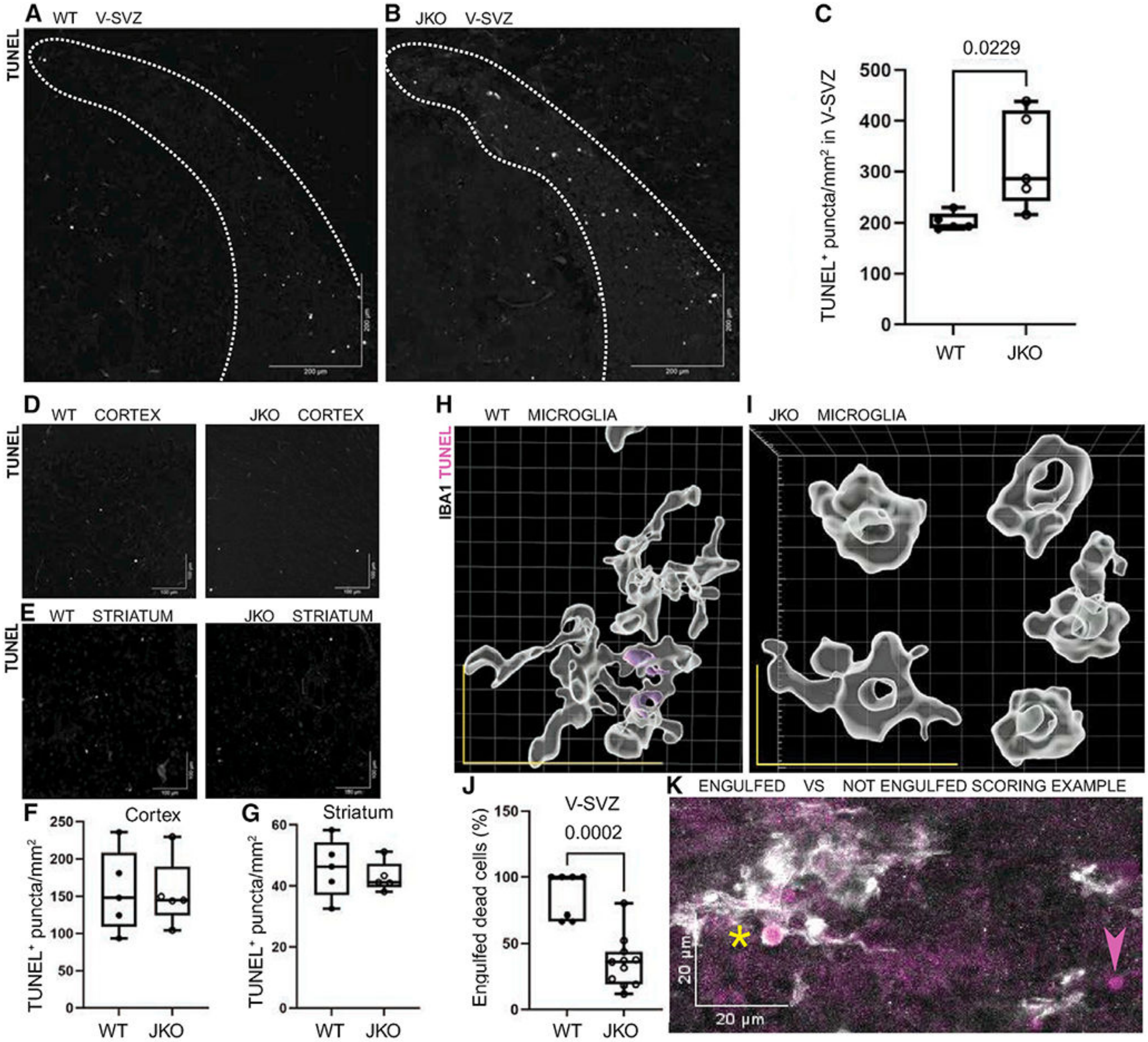

Figure 3. Dead cell number is increased in the V-SVZ of Jedi-deficient mice

(A and B) Representative images of dead cells (TUNEL$^+$ puncta, white) in the V-SVZ (inside the dotted line) of WT (A) and JKO (B). Scale bars, 200 μm.

(C) Quantification of TUNEL$^+$ puncta normalized to the area of the V-SVZ. WT, n = 5 mice; JKO, n = 5 mice.

(D–G) Representative images and quantification of dead cells normalized to the size of the field of view in the cortex (D and F) and striatum (E and G) of WT and JKO. Scale bars, 100 μm. WT, n = 5 mice; JKO, n = 5 mice.

(H and I) 3D-rendering of WT (H) and JKO (I) microglia (IBA1, white) and dead cells (TUNEL, magenta). Scale bars: vertical, 300 pixels; horizontal, 600 pixels.

(J) Quantification of the percentage of dead cells that are engulfed by V-SVZ microglia normalized to the volume of the V-SVZ. WT, n = 4 mice; JKO, n = 6 mice.

(K) Representative maximum-intensity projection of labeling for IBA1 and TUNEL, demonstrating how dead cells were scored as “engulfed” (yellow asterisk) or “not engulfed” (magenta arrowhead). The scoring was done with the image as a z stack. Scale bar, 20 μm.

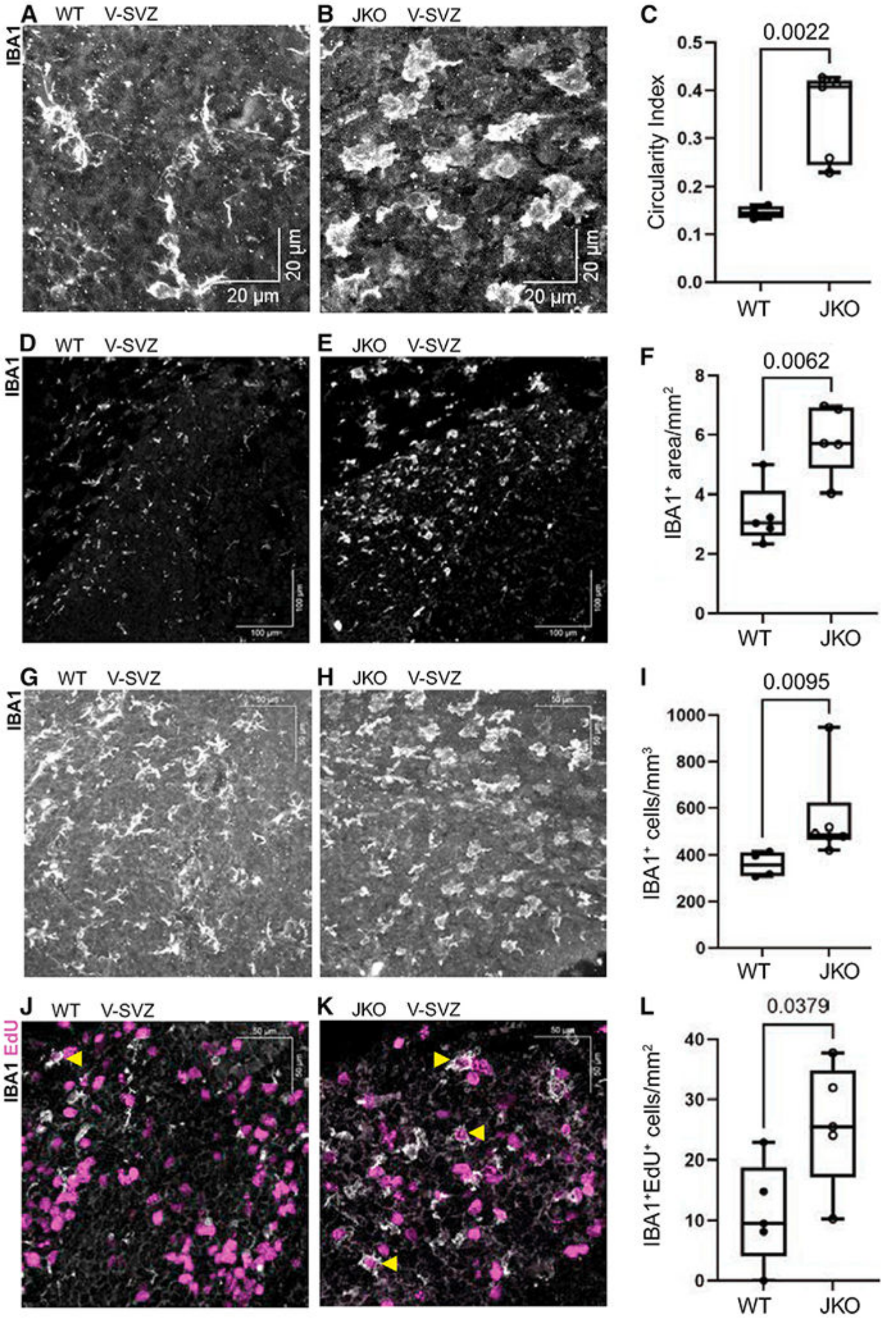

Figure 4. Jedi-deficient microglia adopt an activated phenotype characterized by increased proliferation and ameboid morphology

(A and B) Representative maximum-intensity projections showing the morphology of IBA1$^+$ microglia in WT (A) and JKO (B) V-SVZ. Scale bars, 20 μm.

(C) Quantification of microglia morphology with the circularity index (4π[area]/[perimeter]^2), where higher values indicate an ameboid morphology. WT, n = 4 mice; JKO, n = 5 mice.

(D and E) Representative immunofluorescence images from WT (D) and JKO (E), showing IBA1-labeled area in the V-SVZ. Scale bars, 100 μm.

(F) Quantification of IBA1-labeled area normalized to the area of the V-SVZ. WT, n = 5 mice; JKO, n = 5 mice.

(G and H) Representative maximum-intensity projections showing IBA1$^+$ microglia abundance in WT (G) and JKO (H) V-SVZ. Scale bars, 50 μm.

(I) Quantification of the number of microglia normalized to the area of the V-SVZ. WT, n = 4 mice; JKO, n = 6 mice.

(J and K) Representative immunofluorescence images of proliferating microglia (EdU$^+$IBA1$^+$, yellow arrowheads) in WT (J) and JKO (K) V-SVZ. Scale bars, 50 μm.

(L) Quantification of the number of EdU$^+$IBA1$^+$ microglia. WT, n = 5 mice; JKO, n = 5 mice.

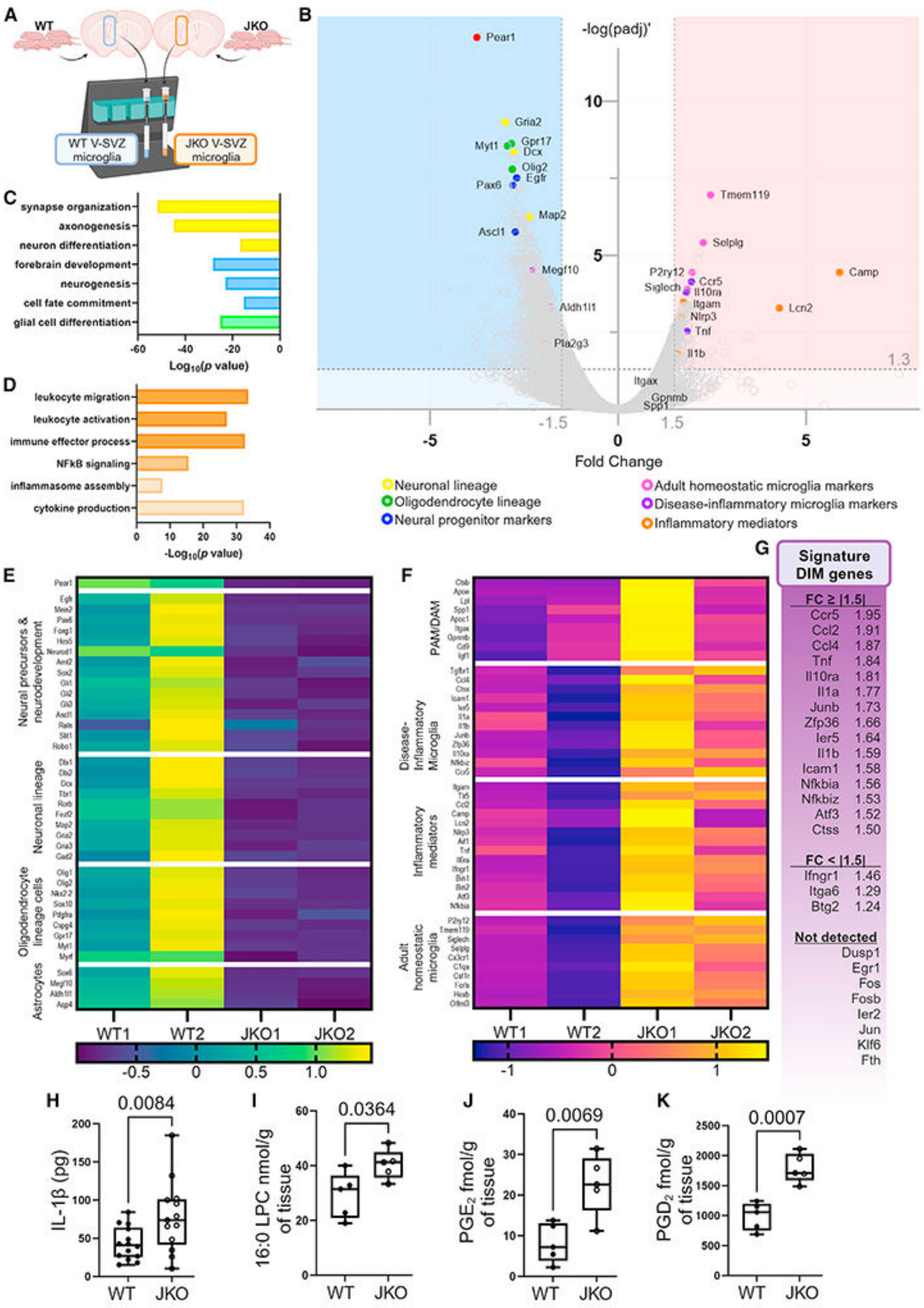

Figure 5. RNA sequencing and lipid and cytokine analyses indicate an increase in inflammatory pathway activation in Jedi-deficient V-SVZ microglia

(A) Illustration of experimental design for comparing WT and JKO V-SVZ microglia transcriptomes.

(B) Volcano plot showing genes that are upregulated (right side, pink shaded) and downregulated (left side, blue shaded) in JKO V-SVZ microglia relative to those in WT V-SVZ. Threshold for statistical and biological significance: adjusted p value ≤0.05 ($-\log(p_{adj})'$ ≥ 1.3) and fold change ≥|1.5|.

(C and D) Histograms showing select gene ontology pathways that are under-represented (C) and over-represented (D) in JKO V-SVZ microglia relative to those in WT.

(E) Heatmap with *Z* scores of select genes with reduced abundance in JKO V-SVZ microglia relative to those in WT.

(F) Heatmap with *Z* scores of select genes that are associated with relevant, previously identified microglia identities and inflammatory pathways and that are upregulated in JKO V-SVZ microglia relative to those in WT.

(G) List of 25 DIM markers, 15 of which are upregulated in JKO V-SVZ microglia relative to those in WT.

(H–K) Quantification of interleukin-1β (IL-1β) (H), 16:0 lysophosphatidylcholine (LPC) (I), prostaglandin E_2 (PGE_2) (J), and prostaglandin D_2 (PGD_2) (K) in microdissected V-SVZ of WT and JKO. In (H), WT n = 14 mice, JKO n = 13 mice; in (I)–(K), WT n = 5 mice, JKO n = 5 mice.

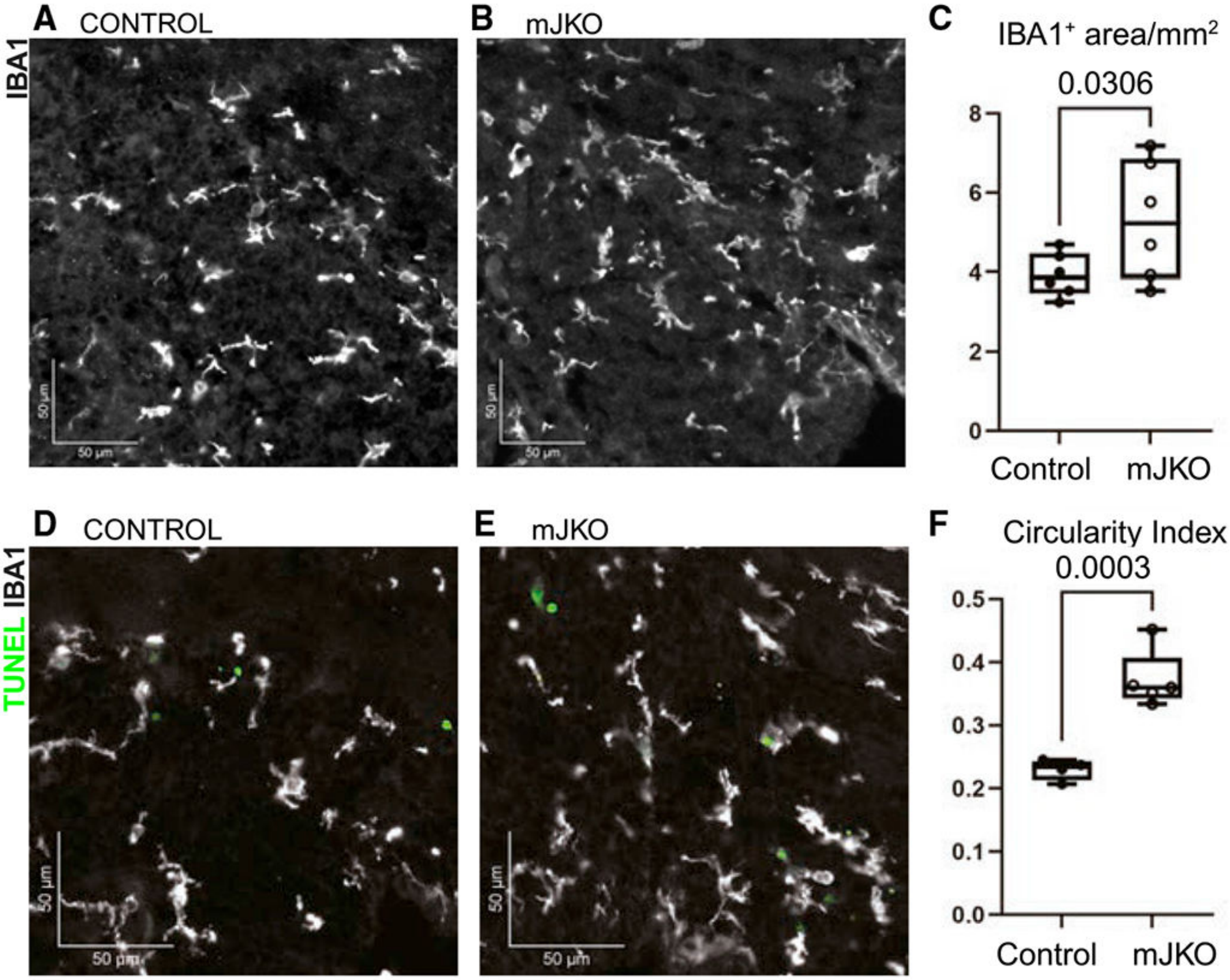

Figure 6. Microglia in the V-SVZ of *Cx3cr1*^{CreERT2};*Jedi*$^{flox/flox}$ mice show evidence of a shift toward a pro-inflammatory phenotype

(A and B) Representative immunofluorescence images of IBA1$^+$ microglia in the V-SVZ of control littermates (A) and mJKO animals (B). Scale bars, 50 μm.

(C) Quantification of IBA1-labeled area normalized the area of the V-SVZ. CTRL, n = 6 mice; mJKO, n = 6 mice.

(D and E) Representative immunofluorescence images of microglia and dead cells (green) in the V-SVZ of controls (D) and mJKO (E). Scale bars, 50 μm.

(F) Quantification of microglia morphology in the V-SVZ using the circularity index. CTRL, n = 4 mice; mJKO, n = 5 mice.

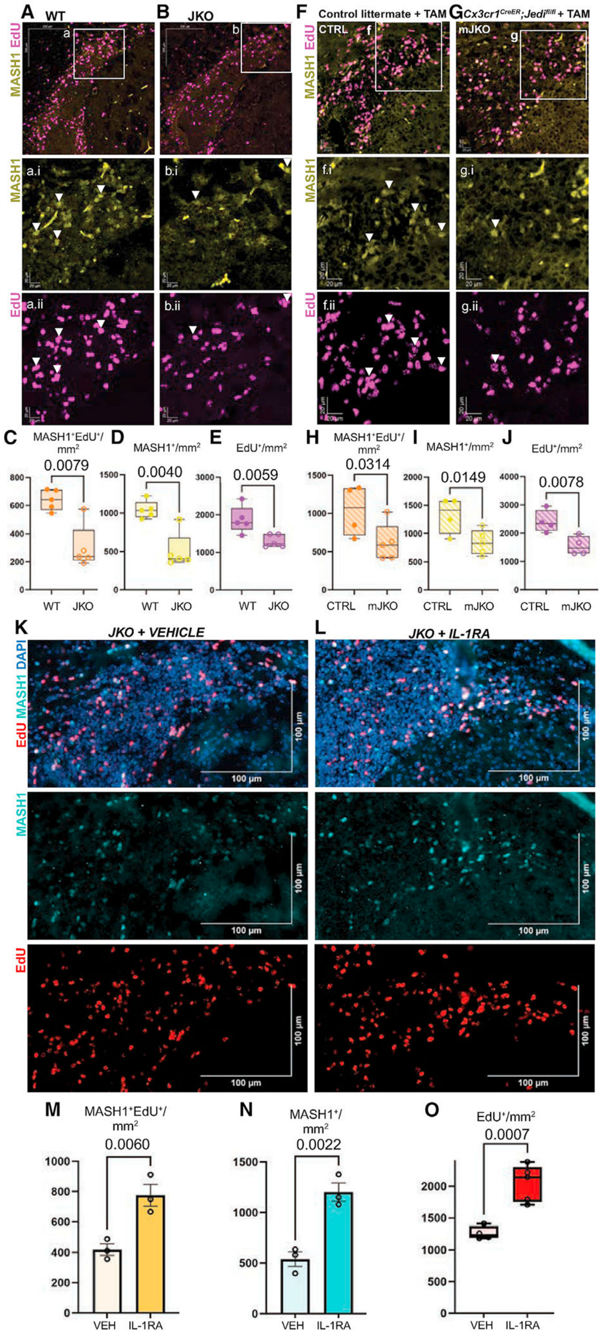

Figure 7. Loss of Jedi (complete or microglial-specific) results in reduced neural precursor proliferation in the V-SVZ, which can be rescued by inhibition IL-1 receptor signaling

(A and B) Representative immunofluorescence images showing proliferating NPCs in WT (A) and JKO (B) V-SVZ. Scale bars, 200 μm. Insets of the NPC marker MASH1 and the proliferation marker EdU^{+} show double-labeled cells (white arrowheads) for WT (a.i and a.ii) and JKO (b.i and b.ii). Scale bars, 20 μm.

(C–E) Quantification of the number of proliferating NPCs (C), total number of NPCs (D), and the number of proliferating cells (E) in the V-SVZ of WT and JKO. WT, n = 5 mice; JKO, n = 5 mice.

(F and G) Representative immunofluorescence images showing proliferating NPCs in the V-SVZ of control (F) and mJKO (G) animals that received tamoxifen (TAM) via their mother. Scale bars, 20 μm. Insets of the NPC marker MASH1 and the proliferation marker EdU$^+$ show double-labeled cells (white arrowheads) for control (f.i and f.ii) and JKO (g.i and g.ii). Scale bars, 20 μm.

(H–J) Quantification of the number of proliferating NPCs (H), total number of NPCs (I), and the number of proliferating cells (J) in the V-SVZ of controls and mJKO. In (H) and (I), CTRL n = 4 mice, mJKO n = 5 mice; in (J), CTRL n = 4 mice, mJKO n = 4 mice.

(K and L) Representative immunofluorescence images showing proliferating NPCs in the V-SVZ of P7 JKO pups that received vehicle (K) or IL-1 receptor antagonist (IL-1RA) (L) at P4. Scale bars, 100 μm.

(M–O) Quantification of the number of proliferating NPCs (M), total number of NPCs (N), and the number of proliferating cells (O) in the V-SVZ of JKO animals that received vehicle (VEH) or IL-1RA. In (M) and (N), JKO + IL-1RA n = 3, JKO + VEH n = 3; In (O), JKO + IL-1RA n = 5, JKO + VEH n = 4.

KEY RESOURCES TABLE

REAGENT or RESOURCE	SOURCE	IDENTIFIER
Antibodies		
Polyclonal Rabbit anti-Mouse IBA1 primary antibody	FUJIFILM Wako Shibayagi	Cat#019–19741; RRID: AB_839504
Monoclonal Mouse anti-Rat MASH1 primary antibody	BD Biosciences	clone 24B72D11.1; Cat#556604; RRID: AB_396479
Polyclonal Sheep anti-Mouse PEAR1 primary antibody	R&D Systems	Cat#AF7607; RRID: AB_2943660
Recombinant Rabbit anti-Mouse TMEM119 antibody [28-3] - Microglial marker	Abcam	Cat#ab209064; RRID: AB_2800343
Polyclonal Donkey anti-Sheep IgG H&L Alexa Fluor 568-conjugated secondary antibody	Abcam	Cat# ab175712; RRID: AB_2892984
Polyclonal Donkey anti-Sheep IgG H&L biotin-conjugated secondary antibody	Invitrogen	Cat#A16045; RRID: AB_2534719
Chemicals, peptides, and recombinant proteins		
Tamoxifen	Sigma-Aldrich	Cat#T5648-1G; CAS: 10540-29-1
Recombinant human IL-1 receptor antagonist protein	R&D Systems	Cat#280-RA
Critical commercial assays		
ApopTag® Fluorescein *In Situ* Apoptosis Detection Kit	Millipore-Sigma	Cat#S7110
Milliplex Mouse Cytokine Magnetic Kit	EMD Millipore	Cat#MCYTOMAG-70K
CD11b (Microglia) Microbeads	Miltenyi Biotec	Cat#130-093-634
Deposited data		
Raw bulk RNA sequencing data	This paper	GEO: GSE232441
Mouse genome assembly GRC38/mm10	Genome Reference Consortium	Mouse Genome Overview - Genome Reference Consortium (nih.gov)
Experimental models: Organisms/strains		
Mouse: Jedi knockout (JKO): Pear1$^{tm1a(KOMP)Wtsi}$	International Mouse Phenotype Consortium	Cat#CSD31459_C05; RRID: MMRRC_060102-UCD
Mouse: Cx3cr1^{CreERT2}: B6.129P2(Cg)-Cx3cr1$^{tm2.1(cre/ERT2)Litt}$/WganJ	The Jackson Laboratory	RRID: IMSR_JAX:021160
Mouse: used to generate the Jedi$^{fl/fl}$ mouse line: B6N.129S4-Gt(ROSA)26Sortm1(FLP1)Dym/J	The Jackson Laboratory	RRID: IMSR_JAX:016226
Oligonucleotides		
Genotyping primers for JKO (Pear1tm1a(KOMP)Wtsi) mice and the floxed Jedi allele: Forward-CTGCCACTGTCATAGCAT	Trevisan et al.[69]	N/A
Genotyping primers for JKO (Pear1tm1a(KOMP)Wtsi) mice and the floxed Jedi allele: Reverse-CACTTAATGACACTCCTT	Trevisan et al.[69]	N/A
Genotyping primers for B6.129P2(Cg)-Cx3cr1$^{tm2.1(cre/ERT2)Litt}$/WganJ: Common primer (Primer 12266)- AAG ACT CAC GTG GAC CTG CT	The Jackson Laboratory	RRID: IMSR_JAX:021160
Genotyping primers for B6.129P2(Cg)-Cx3cr1$^{tm2.1(cre/ERT2)Litt}$/WganJ: Mutant reverse (Primer 14314) - CGG TTA TTC AAC TTG CAC CA	The Jackson Laboratory	RRID: IMSR_JAX:021160
Genotyping primers for B6.129P2(Cg)-Cx3cr1$^{tm2.1(cre/ERT2)Litt}$/WganJ: Wildtype reverse (Primer 16221) - AGG ATG TTG ACT TCC GAG TTG	The Jackson Laboratory	RRID: IMSR_JAX:021160
Quantitative PCR primers for Jedi transcripts: Forward - CAGTTTGATTGCCAGTGCTATG	Trevisan et al.[69]	N/A

REAGENT or RESOURCE	SOURCE	IDENTIFIER
Quantitative PCR primers for Jedi transcripts: Reverse - CCTGTGAACAGGGCACATTA	Trevisan et al.[69]	N/A
Software and algorithms		
TopHat (v2.0.11)	Johns Hopkins University Center for Computational Biology	http://ccb.jhu.edu/software/tophat/index.shtml
DESeq2 (v. 1.34.0)	Love et al.[70]	www.bioconductor.org/packages/release/bioc/html/DESeq2.html
clusterProfiler (v. 4.2.2)	Yu et al.[71]	bioconductor.org/packages/release/bioc/html/clusterProfiler.html
Other		
FluoSpheres™ Carboxylate-modified microspheres (diameter: 2.0 μm)	Invitrogen	Cat#F8826

Table.

SRM Reactions of Lipid Analytes.
(Analyte: Q1 (m/z); Q3 (m/z); C.E.; (polarity))

6-Keto-PGF$_{2\alpha}$: 369.2 (373.2); 163.1 (167.1); −32; (−)
15-HETE: 319.2 (327.2); 169.1 (173.1); −20; (−)
PGF$_{2\alpha}$: 353.2 (357.2); 193.1 (197.1); −34; (−)
PGE$_2$ & D$_2$: 351.2 (355.2); 271.1 (275.1); −23; (−)
PGJ$_2$ & 15-*d*ay-PGD$_2$: 333.2 (337.2); 271.1 (275.1); −22; (−)
15-*day*-PGJ$_2$: 315.2 (319.2); 271.1 (275.1); −25; (−)
2-AG: 379.2 (384.2); 287.2 (287.2); 29; (+)
AEA: 348.2 (352.2); 62.0 (66.0); 24; (+)
AA: 303.1 (311.1); 259.0 (267.0); −15; (−)
OG: 357.2 (362.2); 265.2 (265.2); 23; (+)
OEA: 326.2 (330.2); 62.0 (66.0); 36; (+)
16:0 LPC: 496.4; 184.2; 35; (+)
17:0 LPC: 510.4, 184.2; 35; (+)